ARID1A governs the silencing of sex-linked transcription during male meiosis in the mouse

Debashish U. Menon, Prabuddha Chakraborty, Noel Murcia, & Terry Magnuson*

Department of Genetics, and Lineberger Comprehensive Cancer Center, The University of North Carolina at Chapel Hill, Chapel Hill, NC 27599-7264, USA

*Correspondence: trm4@med.unc.edu, Tel 919-357-2924, Fax 919-843-4682

Abstract

We present evidence implicating the BAF (BRG1/BRM Associated Factor) chromatin remodeler in meiotic sex chromosome inactivation (MSCI). By immunofluorescence (IF), the putative BAF DNA binding subunit, ARID1A (AT-rich Interaction Domain 1a), appeared enriched on the male sex chromosomes during diplonema of meiosis I. Those germ cells showing a Cre-induced loss of ARID1A were arrested in pachynema and failed to repress sex-linked genes, indicating a defective MSCI. Consistent with this defect, mutant sex chromosomes displayed an abnormal presence of elongating RNA polymerase II coupled with an overall increase in chromatin accessibility detectable by ATAC-seq. By investigating potential mechanisms underlying these anomalies, we identified a role for ARID1A in promoting the preferential enrichment of the histone variant, H3.3, on the sex chromosomes, a known hallmark of MSCI. Without ARID1A, the sex chromosomes appeared depleted of H3.3 at levels resembling autosomes. Higher resolution analyses by CUT&RUN revealed shifts in sex-linked H3.3 associations from discrete intergenic sites and broader gene-body domains to promoters in response to the loss of ARID1A. Several sex-linked sites displayed ectopic H3.3 occupancy that did not co-localize with DMC1 (DNA Meiotic Recombinase 1). This observation suggests a requirement for ARID1A in DMC1 localization to the asynapsed sex chromatids. We conclude that ARID1A-directed H3.3 localization influences meiotic sex chromosome gene regulation and DNA repair.

Introduction

Meiosis is central to the formation of haploid gametes from diploid progenitors. During meiosis, homologous chromosomes pair, exchange genetic material, align at the metaphase plate, and then segregate during the first meiotic cell division. Unlike autosomal homologs, the X and Y chromosomes share limited homology. Unique mechanisms have evolved to ensure these chromosomes become sequestered and processed in a parallel but distinct process from autosomes.

XY chromosomes pair along the pseudo-autosomal region (PAR), leaving extensive regions of the X and Y unpaired. These regions become enriched for DNA damage response (DDR) factors, including ATR (Ataxia Telangiectasia and Rad3 related), TOPBP1 (DNA topoisomerase II-binding protein 1), and MDC1 (Mediator of DNA Damage Checkpoint 1), which amplifies γH2A.X across XY chromatin (Alavattam et al., 2022; Ellnati et al., 2017; Fernandez-Capetillo et al., 2003; Ichijima et al., 2011; Royo et al., 2013; Turner et al., 2005). XY chromatin acquires further distinguishing features when the variant histone H3.3 replaces the canonical histones H3.1/3.2, and H3K9me3 (Histone lysine9 trimethylation) becomes elevated on XY chromatin relative to autosomes (Hirota et al., 2018; van der Heijden et al., 2007; Yuen et al., 2014). As the XY chromosomes become epigenetically distinct from autosomes, they also become physically separated into a unique nuclear sub-compartment known as the XY body (Handel, 2004). Transcriptional silencing of unpaired chromatin occurs during this phase of meiosis I, known as meiotic silencing of unpaired chromatin (MSUC) (Turner, 2007). MSUC of autosomal chromatin, such as in response to an abnormal karyotype, causes pachynema arrest and cell death (Baarends et al., 2005; Schimenti, 2005; Turner et al., 2005). However, silencing unpaired XY chromatin results in a different outcome known as meiotic sex chromosome inactivation (MSCI) . Sex chromosomes are required to undergo MSCI and become transcriptionally inactivated. Failure to achieve MSCI triggers arrest and cell death (Ichijima et al., 2011).

Chromatin factors that influence MSCI include the H3K9 methyltransferase, SETDB1 (SET domain, bifurcated 1), PRC1 associated SCML2 (Sex comb on midleg-like protein 2), and testis-specific reader of histone acetylation, BRDT (Bromodomain testis-specific protein) (Hasegawa et al., 2015; Hirota et al., 2018; Manterola et al., 2018). Previous studies demonstrated a critical requirement for SWI/SNF-directed transcriptional regulation during meiosis (Kim et al., 2012; Menon et al., 2019; Wang et al., 2012). The germ cell-specific depletion of the SWI/SNF

68 catalytic subunit, BRG1(Brahma-related gene-1), resulted in an early pachytene arrest (Kim et
69 al., 2012). BRG1 is associated with the XY body (Wang et al., 2012), but its requirement for
70 MSCI is unknown. This lack of evidence for MSCI is also true for the PBAF (POLYBROMO1-
71 BRG1/BRM Associated Factor) remodeler within the SWI/SNF family, which we have shown is
72 required for meiotic cell division (Menon et al., 2021). Whether these data suggest a role for
73 PBAF in MSCI remains an open question, given that BRG1 associates with both SWI/SNF
74 remodelers, PBAF and BAF.

75 Here, we find that ARID1A (AT-rich Interaction Domain 1a), a BAF-specific putative DNA
76 binding subunit, is required for the transcriptional silencing of the sex chromosomes during
77 pachynema, thereby ensuring meiotic progression through prophase-I. Mechanistically, ARID1A
78 is necessary to establish MSCI hallmarks, such as the eviction of elongating RNA polymerase-II
79 (phosphorylated on Serine2 of carboxy-terminal domain; pSer2-RNAPII), limited sex-linked
80 chromatin accessibility, and hyper-accumulation of histone H3.3 on the sex body. Additionally,
81 ARID1A is required for the targeted localization of DMC1 to the unpaired sex chromatids,
82 implicating BAF-A-governed sex-linked chromatin dynamics in DNA repair.
83

84 **Results**
85

86 **Meiotic progression requires ARID1A**

87 Meiotic progression in male mice depends on SWI/SNF-regulated gene expression (Menon et
88 al., 2019; Menon et al., 2021). These studies raise the prospect of distinct SWI/SNF
89 subcomplexes governing stage-specific meiotic transcription (Menon et al., 2021). To
90 understand the meiotic functions of the biochemically distinct SWI/SNF BAF subcomplex, we
91 examined the spermatogenic expression profiles of the BAF subunits *Arid1a* and *Arid1b* using
92 single-cell RNA-seq data generated from testes (Ernst et al., 2019). *Arid1a* mRNA expression
93 occurred at various spermatogenic stages with notable expression at pachynema of meiotic
94 prophase I (Fig. S1A-C).
95

96 *Arid1b* mRNA went undetectable until late in spermiogenesis (Fig. S1A, D-E). Consistent with its
97 mRNA expression profile, pachytene spermatocytes featured abundant ARID1A protein, which
98 was uniformly spread among autosomes and sex chromosomes (Fig. 1). Late in diplonema,
99 ARID1A appeared preferentially enriched on the sex chromosomes as compared to autosomes

100 (Fig. 1). These data implicate ARID1A in meiotic sex chromosome inactivation (MSCI), a
101 process essential for meiotic progression in males.
102
103 To determine whether meiotic spermatocytes require ARID1A, we generated a germ cell-
104 specific knock-out of *Arid1a* using the *Stra8-Cre* transgene expressed in spermatogonia
105 (Sadate-Ngatchou et al., 2008). *Stra8-Cre* was chosen among the available germ-cell-specific
106 Cre lines to circumvent *Arid1a* haploinsufficiency during embryonic development. *Stra8-Cre*
107 remains inactive during embryonic development when transmitted through females (Sadate-
108 Ngatchou et al., 2008). The number of undifferentiated spermatogonia that stained positive for
109 Promyelocytic leukemia zinc finger ($PLZF^+$, also known as Zinc finger and BTB domain
110 containing 16: ZBTB16) remained unchanged in $Arid1a^{cKO}$ testes (Table S1). The proportions of
111 undifferentiated spermatogonia (PLZF+) with detectable (ARID1A+) and non-detectable
112 (ARID1A-) levels of ARID1A protein determined by immunostaining on testes cryosections
113 obtained from 1-month old $Arid1a^{fl/fl}$ (control) and $Arid1a^{cKO}$ (CKO) males was 74% $ARID1A^-$
114 (CKO, n = 179) and 26% $ARID1A^+$ (CKO, n = 65) as compared to 95% $ARID1A^+$ (n = 88) and
115 5% $ARID1A^-$ (n = 5) in controls. Western blot analysis also showed a significant reduction in
116 ARID1A protein in mutant pachytene spermatocytes (Fig. S2). Therefore, the *Arid1a* conditional
117 knockouts generated with a *Stra8-Cre* did not appear to impact earlier stages of
118 spermatogenesis. Potential defects early in spermatogenesis might occur with an earlier-acting
119 germline Cre transgene. In this case, an inducible Cre transgene would be needed, given the
120 haploinsufficiency associated with *Arid1a*.
121
122 Contrary to our expectations, meiosis appeared unperturbed, as evidenced by seminiferous
123 tubules featuring round and elongated spermatids in $Arid1a^{cKO}$ testes (Fig. S3A). Furthermore,
124 $Arid1a^{cKO}$ epididymis featured mature spermatozoa, suggesting that $Arid1a^{cKO}$ testes are
125 capable of normal spermatogenesis (Fig. S3B). Although these data indicate that ARID1A is
126 dispensable for spermatogenesis, we wanted to confirm that these results were not a technical
127 artifact arising from inefficient *Stra8-Cre* mediated excision of the $Arid1a^{fl}$ allele.
128
129 To address this question, we examined *Arid1a* transcripts isolated from $Arid1a^{WT}$ and $Arid1a^{cKO}$
130 Sta-Put purified populations of pachytene spermatocytes and round spermatids using RT-PCR
131 (Fig. S4A). For cDNA synthesis, we used primers that amplify a 612 bp region spanning the

132 *Arid1a* floxed exons 5 and 6. Assuming 100% CRE efficiency, we would expect to observe a
133 281 bp cDNA product associated with mRNA isolated from *Arid1a*^{cKO} spermatogenic cells.
134 Instead, we observed cDNAs representative of the floxed (*fl*) allele and, to a greater extent, the
135 excised (Δ) allele from mRNA isolated from *Arid1a*^{cKO} pachytene spermatocytes. These results
136 indicated inefficient CRE activity (Fig. S4A). More importantly, the data suggest that a fraction of
137 pachytene spermatocytes in *Arid1a*^{cKO} testes fail to undergo CRE-mediated excision, resulting in
138 escapers. An examination of ARID1A levels in testes cryosections and meiotic spreads by
139 immunofluorescence (IF) revealed a heterogenous population of pachytene spermatocytes
140 consisting of mutants lacking and escapers expressing ARID1A (Fig. S4B, C). On average, 70%
141 of pachytene spermatocytes were observed lacking detectable levels of ARID1A signal by IF.
142
143 Furthermore, examining the meiotic profile associated with *Arid1a*^{cKO} revealed an accumulation
144 of mutant spermatocytes (ARID1A^{-}), some at leptonema and zygonema and a majority at mid-
145 pachynema relative to *Arid1a*^{WT} spermatocyte spreads (Table 1). Some diplotene
146 spermatocytes displaying a moderate reduction in ARID1A levels occurred in *Arid1a*^{cKO} relative
147 to *Arid1a*^{WT} meiotic spreads and represent escapers due to inefficient *Stra8-Cre* activity (Table 1
148 - bottom two lines with asterisks, also Fig. S4B,C). However, diplotene and metaphase-I
149 spermatocytes lacking ARID1A protein by IF were undetectable in the *Arid1a*^{cKO} testes (Fig.
150 S4B). These results indicate that those spermatocytes lacking ARID1A arrest at the mid-
151 pachytene stage. The spermatocytes that escape Cre activity progress to subsequent meiotic
152 stages, giving rise to genotypically normal gametes. All round spermatids isolated from
153 *Arid1a*^{cKO} testes appeared only to express the normal transcript associated with the floxed allele
154 (Fig. S4A). Furthermore, our evaluation of the first round of spermatid development based on
155 DNA content (1C, 2C, and 4C), revealed a significantly reduced abundance of round spermatids
156 (1C) in mutant testes compared to wild-type testes. This finding, obtained through flow
157 cytometry, supports the observed meiotic block at the pachytene stage (Fig. S5A-B). Therefore,
158 the perceived lack of a phenotype is an artifact of inefficient *Stra8-Cre* activity. But more
159 importantly, the data indicate that ARID1A is essential for progression beyond pachynema.
160
161 **ARID1A regulates the transcriptional silencing of the sex chromosomes at pachynema**
162 The meiotic requirement of ARID1A and, more importantly, its association with the sex
163 chromosomes at diplonema prompted us to examine its role in MSCI. We hypothesized that

164 ARID1A might play a role in the transcriptional silencing of the sex-linked genes during meiosis.
165 To address this question, we performed RNA-seq on Sta-Put purified populations of pachytene
166 spermatocytes to profile changes in transcript abundance upon ARID1A deficiency. Differential
167 analysis of gene expression using DeSeq2 (Love et al., 2014) revealed an equal proportion of
168 significantly (FDR < 0.05) misexpressed genes displaying either elevated (up-regulated, n=
169 5824) or reduced (down-regulated, n=5821) transcript abundance in *Arid1a*^{cKO} relative to
170 *Arid1a*^{WT} pachytene spermatocytes (Fig. 2A). Notably, we detected significant misexpression of
171 53% of all the sex-linked coding genes (593/1105) in response to an ARID1A deficiency.
172 Amongst these, 86.4% displayed elevated expression (n=512), whereas only 13.6% displayed
173 reduced (n=81) transcript abundance. This skew was even greater when only considering sex-
174 linked genes misexpressed by a magnitude of 2 LOG-fold or higher. Here, 97% (297/306) of the
175 misexpressed sex-linked genes displayed increased transcript abundance in response to an
176 ARID1A deficiency. Therefore, ARID1A predominantly affects the repression of sex-linked
177 genes during pachynema.
178
179 An examination of changes in the average transcript abundance on a chromosome-wide basis
180 showed that expression from the sex chromosomes was significantly higher than that from
181 autosomes in response to the loss of ARID1A at pachynema (Fig. 2B). Therefore, ARID1A
182 regulates the transcriptional repression of the sex chromosomes, implicating it in MSCI.
183 ARID1A's influence on sex-linked gene regulation may result from its association with the sex
184 chromosomes, particularly during diplonema, where ARID1A hyper-accumulates on the XY.
185 However, during pachynema, when MSCI initiates, ARID1A associates with the XY at
186 autosomal levels as detected by IF (Fig. 1). Therefore, it is possible that, at the onset of
187 pachynema, local ARID1A association rather than chromosome-wide coating dictates its role in
188 sex-linked gene repression.
189
190 To address ARID1A's association with the XY chromosomes, we determined its genomic
191 localization at a higher resolution by CUT&RUN (Cleavage Under Targets & Release Using
192 Nuclease) in pachytene spermatocytes. We detected ARID1A occupancy at promoters of
193 differentially regulated target genes, irrespective of their chromosomal location, in *Arid1a*^{WT}
194 relative to *Arid1a*^{cKO} (negative control) pachytene spermatocytes (Fig. S6). This result is
195 consistent with the genome-wide distribution of ARID1A observed in pachytene spermatocyte
196 spreads by IF (Fig. 1). Although not detectable by IF, pachytene spermatocytes displayed a

197 preferential association of ARID1A with promoters of normally repressed sex-linked genes,
198 when detected by CUT&RUN (Fig. S6B), emphasizing its role in MSCI.
199
200 **ARID1A does not influence DNA damage response signaling on the sex body**
201 Unlike autosomal homologs that complete pairing during pachynema, the non-homologous
202 regions of the sex chromosomes feature unrepaired DNA double-strand breaks (DSBs). These
203 DNA DSBs recruit γH2Ax, a product of DNA damage response (DDR) signaling pathways
204 essential for establishing and maintaining MSCI (Turner, 2007). Therefore, to determine
205 whether ARID1A regulated MSCI by influencing DDR signaling, we first monitored the
206 association of γH2Ax with the sex chromosomes in response to the loss of ARID1A. By IF,
207 γH2Ax accumulation on the sex body appeared unperturbed in the mutant (ARID1A^{-}) relative to
208 escapers (ARID1A^{+}) and *Arid1a*^{WT} pachytene spermatocytes (Fig. S7A). Consistent with this,
209 the recruitment of ATR (Ataxia Telangiectasia and Rad3 related), a kinase known to
210 phosphorylate γH2Ax and initiate MSCI (Royo et al., 2013; Turner et al., 2004), appeared
211 normal in the absence of ARID1A. These data indicate that sex-linked DDR signaling occurred
212 independently of ARID1A (Fig. S7B). As expected, MDC1 (Mediator of DNA damage
213 Checkpoint 1), a known γH2Ax reader that is essential for sex body formation
214 (Ichijima et al., 2011), remained associated with the asynapsed sex chromosomes upon
215 ARID1A deletion during pachynema (Fig. S7C). These data indicate that the failure to silence
216 sex-linked genes in response to a loss in ARID1A occurred in the presence of major DDR
217 signaling factors known to govern sex body identity. It is possible that DDR signaling recruits
218 BAF-A to the sex chromosomes.
219
220 **ARID1A limits RNAPII localization to the sex chromosomes during pachynema**
221 Apart from γH2Ax, the association of the sex chromosomes with RNA polymerase II (RNAPII)
222 distinguishes the sex body from the autosomes during pachynema. Normally, pachytene
223 spermatocytes display reduced levels of RNAPII on the sex body relative to autosomes (Khalil
224 et al., 2004). This sub-nuclear localization of RNAPII coincides with increased transcriptional
225 output, which peaks at diplonema (Ernst et al., 2019), underscoring the importance of targeted
226 mechanisms regulating sex chromosome repression. Therefore, we were curious to test
227 whether ARID1A influenced the nuclear localization of RNAPII during pachynema. We
228 performed IF to monitor the localization of the actively transcribing (elongating) form of RNAPII
229 marked by Serine2 phosphorylation (pSer2) on its carboxy-terminal domain (Noe Gonzalez et

230 al., 2021). We monitored elongating RNAPII (pSer2) because its pausing regulates meiotic
231 transcription (Alexander et al., 2023). By co-staining for RNAPII (pSer2) and SYCP3, we could
232 stage pachynema and identify the sex chromosomes. While RNAPII (pSer2) localization to the
233 autosomes appeared similar, we noticed increased levels of RNAPII (pSer2) association with
234 the sex chromosomes in *Arid1a*^{cKO} relative to *Arid1a*^{WT} mid and late pachytene spermatocytes
235 (Fig. 3A). By quantifying the RNAPII (pSer2) signal generated by IF, we detected a 1.5-fold
236 increase (p=0.0003) in the average RNAPII (pSer2) fluorescence associated with the sex
237 chromosomes in *Arid1a*^{cKO} relative to *Arid1a*^{WT} pachytene spermatocytes (Fig. 3B).
238
239 Due to technical difficulties, we could not simultaneously stain for ARID1A alongside SYCP3
240 and RNAPII (pSer2), making distinguishing escapers from mutants in the *Arid1a*^{cKO} meiotic
241 spreads impossible. This result suggests that the 1.5-fold increase in RNAPII association with
242 the sex body in *Arid1a*^{cKO} relative to *Arid1a*^{WT} pachytene spermatocytes is likely underestimated.
243 Therefore, our results indicate that ARID1A facilitates sex-linked gene repression by limiting the
244 association of elongating RNAPII with the sex chromosomes during pachynema.
245
246 **ARID1A regulates promoter accessibility during pachynema**
247 Next, we hypothesized that ARID1A-governed chromatin remodeling might underlie its role in
248 limiting RNAPII accessibility on pachytene sex chromosomes. Therefore, we profiled changes in
249 chromatin accessibility in response to the loss of ARID1A using ATAC-seq. Normally, ATAC-seq
250 peaks (accessible chromatin) are mapped comparably across promoters (34%), intergenic
251 (22.8%), and intronic (21.5%) regions. In contrast, the loss of ARID1A resulted in a dramatic
252 shift towards predominantly promoter-associated ATAC-seq peaks with only a minority mapping
253 to intergenic and intronic regions (Fig. 4A).
254
255 Consistent with an increase in the proportion of promoter-associated peaks, we detected an
256 increase in accessibility across transcription start sites (TSS) associated with both autosomal
257 and sex-linked differentially expressed genes (DEG's) in *Arid1a*^{cKO} relative to *Arid1a*^{WT}
258 pachytene spermatocytes (Fig. 4B,C). Furthermore, in the case of autosomal targets, chromatin
259 accessibility at their TSSs was enhanced irrespective of their transcriptional status, appearing
260 indistinguishable between down-regulated and up-regulated genes upon the loss of ARID1A
261 (Fig. 4B). In contrast, on the sex chromosomes, the loss of ARID1A seemed to have a
262 prominent effect on TSS's associated with up-regulated genes, which displayed greater

263 chromatin accessibility relative to their down-regulated counterparts (Fig. 4C). Therefore, the
264 increased promoter accessibility of normally repressed sex-linked genes may underlie their
265 persistent transcription by RNAPII upon the loss of ARID1A. Overall, these data highlight a role
266 for BAF complexes in limiting promoter accessibility, especially on the sex chromosomes during
267 pachynema.
268
269 **ARID1A regulates the chromatin composition of the sex body**
270 Chromatin remodelers regulate DNA accessibility by altering nucleosome positioning or
271 composition (Clapier et al., 2017). The latter outcome is interesting in the context of MSCI, given
272 that the sex body typically displays a striking enrichment of the variant histone H3.3 while
273 concomitantly appearing depleted of the canonical histones H3.1/3.2 (van der Heijden et al.,
274 2007; Yuen et al., 2014). Given that human ARID1A regulates H3.3 genomic associations
275 (Reske et al., 2022), we tested whether a similar mechanism governed H3.3 localization to the
276 sex chromosomes. To address this, we monitored H3.3 localization in pachytene spermatocytes
277 by IF, simultaneously staining for ARID1A and HORMAD1. The former aided in mutant
278 identification, while the latter labeled the pachytene sex chromosomes. Consistent with previous
279 reports, H3.3 preferentially coats the sex chromosomes, distinguishing it from autosomal
280 chromatin during normal pachynema (Fig. 5A). Interestingly, this sex-body association of H3.3
281 was detected less frequently early in pachynema (17%), becoming more pervasive during the
282 mid (70 %) and late (95%) stages of pachynema. In contrast, in the absence of ARID1A, H3.3
283 staining on the sex chromosomes was indistinguishable from their autosomal counterparts
284 throughout pachynema (Fig. 5A). Notably, the majority of mutant mid (89%) and late (77%)
285 pachytene spermatocytes lacked the typical sex body enrichment of H3.3 (Fig. 5A), indicating
286 that ARID1A dictates the preferential accumulation of H3.3 on the sex body.
287
288 Next, we were curious to know the consequence of reduced H3.3 association on H3.1/3.2
289 occupancy on the sex body in response to the loss of ARID1A. We performed IF to monitor the
290 association of H3.1/3.2 with the sex chromosomes marked by HORMAD1 in response to the
291 loss of ARID1A. Like H3.3, canonical H3.1/3.2 appeared uniformly distributed genome-wide in
292 most early pachytene spermatocytes (92%). At the onset of pachynema, sex chromosomes
293 mostly displayed comparable H3.3 and H3.1/3.2 levels (Fig. 5A, B). However, this balance
294 changed during the subsequent sub-stages of pachynema. Although robust H3.3 levels
295 remained, H3.1/3.2 appeared excluded from the sex chromosomes in most mid (56%) and all

296 late pachytene spermatocytes (Fig. 5A, B). In contrast, the loss of ARID1A increased the
297 proportion of mid (66%) and late (40%) pachytene spermatocytes retaining H3.1/3.2 on sex-
298 linked chromatin (Fig. 5B). The abnormal retention of canonical H3.1/3.2 coincides with a lack of
299 H3.3 enrichment on sex-linked chromatin in response to the loss of ARID1A.
300
301 To determine whether these abnormal kinetics result from a genome-wide deficiency in H3.3,
302 we compared its levels by Western blotting to find no difference in H3.3 abundance in *Arid1a*^{cKO}
303 relative to *Arid1a*^{WT} spermatocyte enriched populations (Fig. S8A). We also considered an
304 alternative possibility that ARID1A might promote the sex-linked enrichment of H3.3 by
305 influencing the expression of cognate chaperones like DAXX and HIRA during murine
306 pachynema (Rogers et al., 2004; van der Heijden et al., 2007). We addressed this by monitoring
307 DAXX and HIRA levels in response to the loss of ARID1A using IF. In the case of DAXX, we
308 examined meiotic spreads to find no changes in either the overall levels or sex chromosome
309 localization of DAXX in response to the loss of ARID1A (Fig. S8B). The same was also true of
310 HIRA, whose levels and nuclear localization in mutants appeared comparable to that seen in
311 escaper (from *Arid1a*^{cKO}) and normal (*Arid1a*^{WT}) spermatocytes (Fig. S8C). Therefore, ARID1A
312 impacts H3.3 accumulation on the sex chromosomes without affecting its expression during
313 pachynema. Overall, our data suggest that ARID1A influences MSCI by regulating the
314 composition of sex-linked chromatin.
315
316 **ARID1A prevents the promoter accumulation of H3.3**
317 To define the changes in the sex-linked associations of H3.3 at a higher resolution, we
318 performed CUT&RUN on pachytene spermatocytes isolated from *Arid1a*^{WT} and *Arid1a*^{cKO} testes.
319 Despite the appearance of a robust H3.3 IF signal from the sex body during normal pachynema
320 (Fig. 5A), the Macs2 peak caller (Zhang et al., 2008) identified very few sex-linked peaks (n =
321 224). These peaks were overwhelmingly associated with intergenic regions (Fig. S9A).
322 Comparatively, a dramatically higher number of peaks (n=12183) primarily associated with
323 genic (promoter, intron, and exon) regions occurred in *Arid1a*^{cKO} pachytene spermatocytes (Fig.
324 S9A). More interestingly, there appeared to be a shift from few but overwhelmingly sex-linked
325 H3.3 peaks (n=224; 98%) to autosomal H3.3 peaks (n=11512; 94.5 %) in response to the loss
326 of ARID1A (Fig. S9A). Additionally, while the proportion of H3.3 sex-linked peaks in *Arid1a*^{cKO}
327 pachytene spermatocytes was few (n=671; 5.5%), they outnumbered their *Arid1a*^{WT}

328 counterparts by 3-fold. These data suggest that the loss of ARID1A strongly influences H3.3
329 genomic associations.
330
331 Due to the increased representation of promoter-associated peaks in response to the loss of
332 ARID1A, we monitored H3.3 association with TSSs of genes differentially regulated by ARID1A.
333 Consistent with the genomic annotation of H3.3 peaks, we could not detect H3.3 enrichment at
334 TSSs associated with ARID1A-regulated sex-linked genes relative to IgG control. H3.3 signal
335 spread gene-wide in *Arid1a*^{WT} pachytene spermatocytes (Fig. S9B, Fig. S10A-top panel). In
336 contrast, we observed a striking accumulation of H3.3 at the TSSs of sex-linked genes
337 misexpressed without ARID1A (Fig. S9B, Fig. S10A). There is a transition from the gene-wide
338 spreading of H3.3 to promoter-proximal enrichment in response to the loss of ARID1A.
339 Concomitantly, X and Y-linked intergenic regions undergo a significant decrease in H3.3
340 occupancy upon ARID1A loss (Fig. S9A). A similar loss of H3.3 occupancy occurred at a
341 handful of autosomal intergenic peaks (Fig. S9A, Fig. S10B - top).
342
343 Unlike the sex-linked targets, TSSs of ARID1A-regulated autosomal genes displayed H3.3
344 enrichment relative to the IgG control (Fig. S9C, Fig. S10B - bottom). However, this TSS
345 occupancy appeared enhanced in *Arid1a*^{cKO} relative to *Arid1a*^{WT} pachytene spermatocytes (Fig.
346 S9C, Fig. S10B). Therefore, TSSs of both sex-linked and autosomal gene targets display
347 concordant changes in H3.3 occupancy. Overall, ARID1A occupancy at TSSs (Fig.S6) of
348 differentially regulated genes prevents the accumulation of H3.3 at target promoters.
349
350 **ARID1A restricts H3.3 occupancy to intergenic regions on the sex chromosomes**
351 Our analysis of the genome-wide localization of H3.3 in response to the loss of ARID1A would
352 argue that the abnormal increase in promoter-associated H3.3 results from its redistribution
353 from high-affinity sites (peaks) that are predominantly sex-linked and intergenic during normal
354 pachynema (Fig. S9A, Fig. S10). We focused our attention on these H3.3-occupied intergenic
355 sex-linked sites. Although the Macs2 algorithm identified only 224 sex-linked intergenic peaks,
356 we speculated that this approach filtered out regions enriched for H3.3 that fail to meet the peak
357 calling threshold compounded by the pervasive spreading of H3.3 on the sex chromosomes
358 (Fig. 5A, Fig. S9B, S10A). We adopted an alternative strategy that involved identifying potential
359 H3.3 bound sites by monitoring their occupancy at ARID1A-governed accessible chromatin (Fig.
360 4A). We compared *Arid1a*^{WT} and *Arid1a*^{cKO} pachytene spermatocyte associated ATAC-seq

361 peaks to identify mutually exclusive and overlapping peaks using BEDTools (Quinlan and Hall,
362 2010). The resulting peaks cluster into lost (n=9), common (n=7194), or gained (n=2246) based
363 on their absence, persistence, or appearance, respectively, in *Arid1a*^{cKO} relative to *Arid1a*^{WT}
364 pachytene spermatocytes (Fig. 6A). Next, we examined the ATAC-seq signal at these regions to
365 find an increase in accessibility not only at gained peaks as expected but also at common peaks
366 in *Arid1a*^{cKO} relative to *Arid1a*^{WT} pachytene spermatocytes.
367
368 Despite being labeled as lost, these regions did not display the expected loss in ATAC-seq
369 signal in *Arid1a*^{cKO} relative to *Arid1a*^{WT} pachytene spermatocytes (Fig. 6A, left panel). The ATAC
370 signal appears unchanged, highlighting the possibility that lost regions were labeled as such
371 because they failed to satisfy Macs2 peak thresholds in *Arid1a*^{cKO} pachytene spermatocytes,
372 especially given the comparatively higher magnitude of ATAC signal surrounding the common
373 and gained peaks (Fig. 6A, left panel). We restricted our analysis to common and gained sites
374 constituting 99 % of sex-linked regions subject to ARID1A-regulated chromatin accessibility.
375 By plotting the average H3.3 coverage at sites associated with common and gained peaks, we
376 detected striking differences in H3.3 occupancy. Briefly, both common and gained open
377 chromatin regions consisted of loci differentiated by either a loss or robust increase in H3.3
378 occupancy in *Arid1a*^{cKO} relative to *Arid1a*^{WT} pachytene spermatocytes (Fig. 6A, right panel). To
379 gain further insight, we performed k-means clustering, based on H3.3 occupancy, to identify 4
380 clusters associated with either common (C1-C4) or gained (G1-G4) peaks (Fig. 6B). The
381 clusters associated with common ATAC-seq peaks displayed contrasting changes in H3.3
382 occupancy in response to the loss of ARID1A. C1 and C2 represented regions deficient for
383 H3.3, while C3 and C4 represent regions that gained H3.3 binding in *Arid1a*^{cKO} relative to
384 *Arid1a*^{WT} pachytene spermatocytes (Fig. 6B, right panel). Similarly, clusters associated with
385 gained ATAC-seq peaks, namely, G1 and G3, represented sites that gained H3.3 occupancy,
386 while G2 identified sites that lost H3.3 occupancy. In contrast to clusters G1-G3, regions
387 associated with G4 displayed an unremarkable association with H3.3 in response to the loss of
388 ARID1A (Fig. 6B, right panel). Genomic annotations of common and gained k-means clusters
389 revealed that the sites that displayed a loss of H3.3 binding (represented by C1 + C2, G2) in
390 response to the loss of ARID1A were intergenic (Fig. S11A).
391
392 In contrast, those that gained significant H3.3 localization (represented by C3, C4, and G1+G3)
393 distributed differentially between intergenic and genic regions (Fig. S11A). Therefore, these data

394 support our idea that ARID1A restricts H3.3 occupancy primarily to intergenic sites on the sex
395 chromosomes. Furthermore, the loss of ARID1A triggers an abnormal redistribution of H3.3 to
396 genic regions. Therefore, the increased promoter occupancy of H3.3 is an indirect consequence
397 of ARID1A loss.
398
399 **ARID1A-governed H3.3 localization influences the sex-linked association of DMC1**
400 To gain further insight into the mechanisms regulating H3.3 associations on the sex
401 chromosomes, we examined the regions associated with various k-means clusters to
402 investigate the enrichment of relevant motifs. To our surprise, we detected an enrichment of the
403 motif associated with the DSB hotspot specifier, PRDM9 (PR domain-containing protein 9), in
404 clusters related to gained peaks, G1 and G3 (Fig. S11B, top). Additionally, we observed an
405 increased frequency of PRDM9 motif centered at gained ATAC-seq peaks associated with G1
406 and G3 (Fig. S11B, middle).
407
408 Interestingly, regions associated with G1 and G3 are usually devoid of H3.3 (Fig. 6B), implying a
409 potential antagonism between H3.3 occupancy and the occurrence of meiotic DNA DSBs.
410 Gained ATAC-seq peaks associated with G2, which usually displays H3.3 occupancy, appeared
411 devoid of PRDM9 motif occurrences relative to G1 and G3 (Fig. S11B, middle). Next, we
412 determined the frequency of the PRDM9 motif at k-means clusters associated with common
413 ATAC-seq peaks. These regions also displayed a dichotomous association with H3.3 (Fig. 6B).
414 C3 and C4, usually deficient in H3.3, showed an increased frequency of PRDM9 motifs relative
415 to C2, which typically displays H3.3 binding (Fig. S11B, bottom). These data illustrate an
416 antagonistic relationship between H3.3 and meiotic DNA DSBs.
417
418 Since the PRDM9 motifs identified from SSDS (Single-Stranded DNA Seq) data were generated
419 to map the genomic associations of DNA repair factor DMC1 (Brick et al., 2012), we monitored
420 its enrichment at the various k-means clusters. We also monitored the association of markers of
421 meiotic DNA DSBs, such as the PRDM9 catalyzed H3K4me3 at common and gained k-means
422 clusters using published ChIP-seq data from pachytene spermatocytes (Maezawa et al.,
423 2018a). Consistent with the motif analyses, DMC1 occupancy and H3K4me3 enrichment
424 occurred at gained and common ATAC-seq peaks associated with k-means clusters, normally
425 devoid of H3.3, namely, G1, G3, G4, C3, and C4 (Fig. S11 C, D).
426

427 These data suggest that ARID1A might indirectly influence DNA DSB repair on the sex
428 chromosomes by regulating the localization of H3.3. To test this conclusion, we monitored the
429 association of DMC1 on the sex chromosomes in response to the loss of ARID1A by IF.
430 Normally, DMC1 foci appear distributed along the non-homologous arms of the X and Y
431 chromosomes from early to mid-pachynema, only disappearing by late pachynema (Fig. 7A, left,
432 panel insets) (Moens et al., 2002). In contrast, in the absence of ARID1A, we observed a
433 marked reduction in the number of DMC1 foci (Fig. 7A, right, panel insets). Quantification of
434 DMC1 foci in Arid1a^{cKO} relative to Arid1a^{WT} pachytene spermatocytes revealed a significant
435 decrease in the sex-linked association of DMC1 in the absence of ARID1A (Fig. 7B). Along with
436 DMC1, the mitotic DNA recombinase, RAD51, is also known to localize to the non-homologous
437 arms of the sex chromosomes (Moens et al., 1997; Moens et al., 2002). Therefore, we
438 determined whether ARID1A also influenced the sex-linked association of RAD51. First, we
439 analyzed previously generated RAD51-SSDS data (Hinch et al., 2020) to monitor its enrichment
440 across the various k-means clusters associated with common and gained ATAC-seq peaks.
441 Unlike DMC1, we found no detectable levels of RAD51 at any k-means clusters (Fig. S12A).
442 Furthermore, the formation of RAD51 foci along the asynapsed axes of the sex chromosomes
443 appeared unchanged in *Arid1a^{cKO}* relative to *Arid1a^{WT}* pachytene spermatocytes (Fig. S12B).
444 Therefore, ARID1A is necessary for the normal sex-linked association of DMC1 but not RAD51.
445 More importantly, our data highlight a dual role for ARID1A in regulating sex chromosome
446 repression and DNA repair (Fig. 8).
447
448 **Discussion**
449 We previously demonstrated a spermatogenic requirement for the mammalian SWI/SNF
450 complex based on its role in coordinating germline transcription (Menon et al., 2019).
451 Furthermore, we showed that the SWI/SNF PBAF subcomplex activates genes essential for
452 reductional meiosis and gamete formation (Menon et al., 2021). These data highlight that
453 distinct SWI/SNF subcomplexes govern specific meiotic transitions.
454
455 Our current study demonstrates a requirement for the ARID1A-associated BAF (BAF-A)
456 subcomplex for meiotic sex chromosome inactivation (MSCI). It does so by promoting the
457 accumulation of the variant histone H3.3 on the sex chromosomes at the onset of mid-
458 pachynema, coinciding with the eviction of canonical histones H3.1/3.2 and RNA polymerase II
459 from the sex body (Model, Fig. 8). In contrast, when depleted of ARID1A, chromatin accessibility

460 increased along with a deficiency of H3.3 and the continued presence of H3.1/3.2 and pSer2-
461 RNAPII (an elongating form of RNA polymerase II) in the sex body. These data indicate that
462 BAF-A helps define features distinguishing sex chromosomes from autosomes and that the
463 absence of the BAF-A subcomplex during meiosis I results in the failure of MSCI during
464 pachynema.
465
466 Although previous work described the association of H3.3 with the sex body (van der Heijden et
467 al., 2007; Yuen et al., 2014) and its requirement for meiotic repression of sex-linked genes
468 (Fontaine et al., 2022), our study revealed the need for BAF-A in the preferential localization of
469 H3.3 to the sex body relative to autosomes. Interestingly, a similar role for BAF-A in promoting
470 H3.3 incorporation occurs in human endometriotic cells (Reske et al., 2022). In this case, the
471 genomic localization of H3.3 to super-enhancers required ARID1A. Our study describes the
472 ARID1A-dependent localization of H3.3 at a chromosome-wide scale comprised of (i) local
473 enrichment at intergenic loci and (ii) larger domains that resembled spreading much like that of
474 *Xist* during female X chromosome inactivation (XCI) (Chaumeil et al., 2006). Interestingly, X
475 chromosome inactivation (XCI) requires SWI/SNF subunits SMARCA4 and SMARCC1 in
476 female mouse embryonic stem cells (mESC) (Keniry et al., 2022). Here, SMARCC1 promotes
477 XCI by increasing promoter accessibility of the inactive X chromosome (Xi). Although sex-linked
478 chromatin accessibility is thought to increase during MACI (Maezawa et al., 2018b), our studies
479 showed that BAF-A serves to limit rather than enhances sex-linked chromatin accessibility at
480 pachynema. These data highlight a mechanism that checks chromosome-wide relaxation during
481 MSCI. The divergent outcomes of SWI/SNF-governed sex-linked chromatin accessibility during
482 XCI and MSCI probably reflect noticeable sex-specific differences or arise from potentially
483 perturbing distinct SWI/SNF subcomplexes.
484
485 Along with altered chromatin composition and structure, pachytene spermatocytes lacking
486 ARID1A also displayed an abnormal association of pSer2-RNAPII (elongating form) with the sex
487 body. Normally, total transcriptional output peaks towards the end of meiotic prophase-I, even
488 with MSCI coinciding (Alexander et al., 2023; Ernst et al., 2019; Monesi, 1964). The dynamic
489 switching from the paused (pSer5-RNAPII) to the elongating (pSer2-RNAPII) state of RNAPII
490 drives this burst of transcription on autosomes (Alexander et al., 2023). The association of
491 pSer2-RNAPII with the sex chromosomes without ARID1A renders them more autosome-like,
492 underlying the defect in sex-linked gene repression. The BAF-A-governed H3.3 dynamics on the

493 sex chromosomes may limit the switch from the paused to the elongating state of RNAPII. In a
494 human cell culture model, ZMYND11, a known tumor suppressor and reader of Lysine 36
495 trimethylation on H3.3 (H3.3K36me3), suppresses RNAPII elongation (Wen et al., 2014).
496 Whether similar H3.3 readers affect RNAPII pausing during meiosis in mice remains unknown.
497
498 The initiation and maintenance of MSCI are known to be regulated by DNA damage response
499 (DDR) factors, ATR, and MDC1, respectively (Ichijima et al., 2011, Royo et al., 2013, Turner et
500 al., 2004. However, ARID1A deficient pachytene spermatocytes appeared proficient in sex-
501 linked DDR signaling, evidenced by the normal enrichment of ATR, γH2Ax, and MDC1 on the
502 sex body. It is possible that BAF-A-mediated transcriptional repression of the sex chromosomes
503 occurs independently of DDR signaling. However, given that the accumulation of ATR and
504 MDC1 on the sex body precedes that of ARID1A, which only manifests late in diplonema, it is
505 reasonable to hypothesize that DDR signaling might recruit BAF-A to the sex chromosomes.
506
507 ARID1A did not appear necessary for sex-linked DNA DSB formation. In contrast, the expected
508 association of DMC1, the meiosis-specific DNA recombinase, with the asynapsed axes of the
509 sex chromosomes do require ARID1A. Interestingly, sex-linked intergenic sites displaying an
510 ARID1A-dependent enrichment of H3.3 appeared depleted for DMC1. Consistent with this
511 antagonism, the loss of ARID1A resulted in the re-distribution of H3.3 to regions normally
512 associated with DMC1. However, a subset of normal DMC1-associated regions (G4) displaying
513 a distinct chromatin composition with little or no occupancy of H3.3 may undergo different
514 dynamics of ARID1A regulation. Although only correlative, these data suggest that regions
515 displaying a localized enrichment of H3.3 might be unfavorable for DNA repair. Determining the
516 extent to which a deficiency in BAF-A activity might impede sex-linked DNA repair is
517 challenging. RAD51 binding to the sex chromosomes remained stable without ARID1A,
518 suggesting that some sex-linked DNA repair remains. Furthermore, RAD51 and DMC1 bind
519 ssDNA at PRDM9/SPO11 designated DSB hotspots. However, these recombinases occupy
520 unique domains. DMC1 localizes nearest the DSB breakpoint, promoting strand exchange,
521 whereas RAD51 is further away (Hinch et al., 2020). Our data suggest that loss of ARID1A
522 decreases DMC1 foci on the XY chromosomes without affecting RAD51. These findings
523 suggest that BAF-A may play a role in the loading and/or retention of DMC1 to the XY
524 chromosomes. Additionally, it would be interesting to monitor the formation of DMC1 and RAD51 foci
525 early in meiosis I (Leptonema-Zygonema) in response to ARID1A loss. However, this analysis would

526 require a conditional mutation of *Arid1a* using a different *Cre* line. Nonetheless, our studies highlight a
527 model in which BAF-A promotes meiotic progression by facilitating MSCI and DNA repair on the
528 sex chromosomes.
529
530 **Materials and Methods**
531
532 **Generation of *Arid1a* conditional mutant mice**
533 Generation of the *Arid1a*^{tm1Mag}/Mmnc mutant allele was previously described (Chandler et al.,
534 2015). The mice are available through the regional mutant mouse resource and research center
535 (MMRRC; Stock number: 041418-UNC; www.mmrrc.org). *Arid1a* floxed mice
536 (*Arid1a*$^{tm1Mag/}$*Mmnc*) exist on a CD1 genetic background. Crosses with testes-specific *Stra8-Cre*
537 mice (expressed in P3 spermatogonia) (Sadate-Ngatchou et al., 2008) resulted in conditional
538 knockouts. *Arid1a*$^{fl/fl}$; *Stra8- Cre*$^{Tg/0}$ females were crossed to either *Arid1a*$^{fl+}$ or *Arid1a*^{flfl} males to
539 obtain *Arid1a*^{flfl};*Stra8-Cre*$^{Tg/0}$ (*Arid1a*^{cKO}) and either *Arid1a*^{flfl} or *Arid1a*$^{fl+}$ (*Arid1a*^{WT}) males.
540 Haploinsufficiency associated with *Arid1a* negated the possibility of transmitting the Cre through
541 the paternal germline. Genotyping primers: *Arid1a*$^{fl+}$ alleles - (F)- 5' -
542 CTAGGTGGAAGGTAGCTGACTGA -3'; (R) 5' - TACACGGAGTCAGGCTGAGC -3' (PCR
543 product sizes- *fl*: 300 bp; *+*: 200 bp), and *Stra8-Cre* - (F) 5' -GTGCAAGCTGAACAACAGGA-3',
544 (R) 5' -AGGGACACAGCATTGGAGTC-3' (PCR product size- *Cre*: 150 bp). Mice were housed
545 with a 12-hour light cycle (temperature - 20-24° C, humidity - 30-70%). All animal work followed
546 approved UNC Chapel Hill IACUC protocols.
547
548 **Histology**
549 *Arid1a*^{WT} and *Arid1a*^{cKO} testes and cauda epididymites were fixed overnight in Bouins solution
550 (Fisher Scientific Ricca chemical; 11-201) at 4° C, followed by dehydration in ethanol series
551 (50%, 70%, and 100%) before embedding in paraffin. The animal histopathology core prepared
552 stained tissue sections (hematoxylin and eosin for cauda epididymites; Periodic acid-Schiff for
553 testes). Staining and morphology determined seminiferous tubule staging (Ahmed and de Rooij,
554 2009; Meistrich and Hess, 2013). A summary of staging is provided (Supplementary Table 2).
555
556 **Immunofluorescence staining of testis cryosection and spermatocyte spreads**
557 Testes cryosections and spermatocyte spreads from juvenile (P18, P19, and P26) and adult
558 *Arid1a*^{WT} and *Arid1a*^{cKO} mice were examined with indirect immunofluorescence (IF). 8-10 µm

559 thick cryosections of testes were prepared using published methods (Menon et al., 2021).
560 Whole testes were fixed in 10% neutral buffered formalin (NBF) at 4° C for 20 minutes. They
561 were cut in half, followed by 40 minutes of incubation in 10% NBF. Fixed tissues were washed
562 three times (10 minutes per wash) in room temperature (RT) phosphate-buffered saline (PBS)
563 pH7.4. The tissues were then treated with a series of sucrose washes - 10% (30 min), 20% (30
564 min), and 30% (1 hr). Tissues were then incubated at 4° C overnight in a 1:1 ratio of a solution
565 of 30% sucrose/optimum cutting temperature (OCT, Tissue-Tek; 62550-01), followed by
566 embedding in OCT, sectioning, and storage at -80^{0} C. Before immunostaining, cryosections
567 were thawed on a heating block at 42^{0} C, rehydrated for 10 minutes in PBS, and incubated in
568 10mM citric acid buffer (pH6.0) for 10 minutes at 80-90^{0} C (antigen retrieval), during which
569 addition of fresh citrate buffer (80-90 ^{0}C) occurred every 2 minutes, and then allowed to cool for
570 20 minutes. For immunostaining, cryosections were incubated overnight in a humidified
571 chamber with primary (Supplementary Table3) at 4^{0} C and then followed by a secondary
572 antibody incubation at RT for 1 hr. Sera were diluted with antibody dilution buffer in PBS (ADB:
573 3% bovine serum albumin; 10% goat serum; 0.5% Triton-X 100). Two identical blocking steps
574 preceded antibody incubations. These steps involved sequential incubations in (i) PBS, (ii)
575 PBS/0.1% Triton-X 100, and (iii) blocking solution (1:10 dilution of ADB in PBS) for 10 minutes
576 each at RT. Immunostained slides were washed twice in Kodak Photo-Flo 200 (PBS/0.32%),
577 counterstained with DAPI, washed again in PBS/0.32% Photo-Flo 200, and then mounted in
578 Prolong Gold antifade medium (P-36931; Life Technologies).
579
580 Spermatocyte spreads were prepared as previously described (Gray et al., 2020) with minor
581 modifications. Briefly, seminiferous tubules were incubated in hypotonic buffer (30mM Tris
582 pH8.2, 50mM Sucrose, 17 mM Trisodium dihydrate, 5mM EDTA, 0.5mM DTT, 0.1 mM PMSF)
583 for 10-20 minutes on ice. Tubules were minced in 100 mM sucrose (200 μL/testis) until the
584 solution turned turbid. The resulting cell suspension was isolated, avoiding tissue debris, and
585 held on ice. Cells were fixed and spread by dropping 20 μL of cell suspension directly onto glass
586 slides coated with paraformaldehyde solution (1 % Paraformaldehyde; 0.15 % Triton X-100; 625
587 nM Sodium Borate, pH 9.2). Uniform spreading was ensured by tilting the slides along the near
588 and opposite edges. Next, slides were incubated in a humidified chamber for 1 hr, following
589 which they quickly air-dried and then washed two times in PBS/0.32% Photo-Flo 200 and once
590 in H_2O/0.32% Photo-Flo 200. Air-dried slides were immediately processed for immunostaining
591 as described above for cryosections or stored at - 80^{0} C. Immunostained spreads were washed

592 2x with PBS/0.32% Photo-Flo 200, counterstained with DAPI, and washed again with Photo-Flo
593 200. Stained spreads were mounted in Prolong Gold antifade medium. The list of antibodies for
594 IF is provided in supplementary table 3. The Leica Dmi8 fluorescent microscope was used to
595 capture images. Z-stacks were deconvoluted using Leica Dmi8 image software (Huygens
596 essentials version 20.04). Some whole immunofluorescence image panels with low visibility
597 (see figure legends 3,5 and supplemental figure legends 4,6,7) were enhanced to increase
598 brightness.
599
600 Fluorescence intensity measurements and object (foci) counting were performed with Fiji
601 (Schindelin et al., 2012). RNAPII (pSer2) IF signal intensities were measured using the method
602 described previously (Menon et al., 2021). Briefly, pixel intensities were recorded from regions
603 of interest (ROI), which include the sex chromosomes (sex body) and an area lacking cells
604 (background fluorescence). Corrected total RNAPII-pSer2 fluorescence (CTRF) was calculated
605 using the method previously described
606 (https://theolb.readthedocs.io/en/latest/imaging/measuring-cell-fluorescence-using-imagej.html),
607 where CTRF= Integrated density associated with sex body – (Area of sex body x Mean
608 fluorescence of background).
609
610 For counting axial DMC1 foci, images were cropped to an area encompassing the sex
611 chromosomes. Cropped images were converted to 8-bit grayscale, and the DMC1 fluorescent
612 channel selected for further processing. An ROI was set, manual thresholding was performed to
613 select DMC foci, and noise (speckles) removed using the Fiji median filter tool with a radius set
614 to 2.0-4.0. Finally, DMC1 was enumerated with the count particles tool. Statistical significance
615 was calculated using an unpaired student's t-test. Metadata associated with the quantification of
616 RNAPII (pSer2) fluorescence and DMC1 foci are provided (Supplementary Table 4,5)
617
618 **Preparation of acid-extracted histones and western blotting**
619 Histones from P19 *Arid1a*^{WT} and *Arid1a*^{cKO} spermatogenic cells were acid-extracted using
620 published methods (Shechter et al., 2007). Seminiferous tubules were digested in 1 mL of
621 Enriched Krebs-Ringer Bicarbonate (EKRB) Medium (EKRB salts - 1.2 mM KH_2PO_4, 1.3 mM
622 $CaCl_2$, 119.4 mM NaCl, 4.8 mM KCl, 1.2 mM $MgSO_4$, 11.1 mM Dextrose; 25.2 mM $NaHCO_3$; 1X
623 essential amino acids -Invitrogen, 11130051; 1X non-essential amino acids-Gibco,11140050)
624 supplemented with 0.5 mg/mL collagenase (10 minutes, rotated at 32 ^{o}C). Digested tubules

625 sedimented by gravity for 5 minutes at RT. The supernatant was removed, tubules were
626 resuspended in 1 mL EKRB medium, and then settled for 5 minutes at RT. The sedimented
627 tubules were transferred to 1 mL EKRB medium supplemented with 0.025% trypsin and 4
628 μg/mL DNase-I. The suspension was incubated for 10 minutes on a rotator at 32° C. Digestion
629 was halted with 10% Fetal bovine serum (FBS), and single-cell suspensions were prepared by
630 pipetting the slurry and then filtering it sequentially through 70 μm and 40 μm filters. Cells were
631 pelleted at 600g for 5 minutes, washed once in PBS, and processed for histone extraction.
632 Briefly, cell pellets were resuspended in 1 mL hypotonic lysis buffer (10mM Tris-Cl pH8.0, 1mM
633 KCl, 1.5mM $MgCl_2$, 1mM DTT) and incubated on a rotator at 4° C for 30 minutes. Nuclei were
634 pelleted at 10,000 g for 10 minutes at 4° C. Nuclear pellets were resuspended in 400 μL 0.2N
635 HCl and incubated for 1 hr at 4 ^{o}C, followed by centrifugation at 14,000 g for 10 minutes at 4° C
636 to isolate supernatants containing histones that were precipitated with Trichloroacetic acid
637 (TCA), and then added to the nuclear suspension at a final concentration of 33% and incubated
638 on ice for 30 minutes. Precipitated histones were pelleted at 14,000g for 10 minutes at 4° C and
639 washed two times in 1 mL ice-cold acetone. Finally, washed histones were air-dried at RT for 20
640 minutes and resuspended in 100 μL ddH_2O. Histones were separated on a 15 % SDS-
641 polyacrylamide gel for Western blots and transferred to a PVDF (Polyvinylidene Difluoride)
642 membrane using a semi-dry transfer apparatus (Bio-Rad). Sample loading was assessed by
643 REVERT™ total protein stain (LI-COR, 926-11010). Blots were scanned on a LI-COR Odyssey
644 CLx imager and viewed using Image Studio Version 5.2.5. Antibodies and their corresponding
645 dilutions are listed (Supplementary Table 3).
646
647 **Isolation of Pachytene Spermatocytes by the Sta-Put Method of Unit Gravity and Western**
648 **Blotting**
649 Pachytene spermatocytes were purified from *Arid1a*^{WT} and *Arid1a*^{cKO} adult testis by the unit
650 gravity sedimentation procedure using a Sta-Put apparatus (Bellvé, 1993; O'Brien, 1993). Testis
651 from at least 12 adult males (>P60) were dissected into EKRB, decapsulated, and digested in
652 0.5mg/ml collagenase for 15 min at 32° C. The resulting tubules were gently washed with EKRB
653 and digested with 0.25mg/ml trypsin supplemented with 4μg/ml DNase for 15 min at 32° C.
654 Following trypsin incubation, additional DNase (4μg/mL) was added to reduce viscosity further.
655 Samples were triturated for 3 minutes with a plastic transfer pipet to fragment flagella, break
656 intercellular bridges between germ cells, and further disperse cells into suspension. Trypsin
657 digestion was stopped by adding 0.25mg/mL trypsin inhibitor (Sigma/EPRO, T9003), and cell

658 aggregates were removed by filtration using 40 μm cell strainers. Cells from the flow-through
659 were pelleted at 500g for 5 min at 4° C, resuspended in EKRB + 0.5% BSA, and adjusted to a
660 3.33×10^8 cells/mL density. 10^9 cells from this single-cell suspension were loaded onto a 2-4%
661 linear BSA gradient and allowed to sediment in the Sta-Put apparatus at 4° C. After 2hr and
662 40min of undisturbed sedimentation, 10ml fractions were collected at 45 sec per tube. Fractions
663 were pelleted at 500g for 5 min at 4°C and resuspended in 1ml EKRB + 0.5%BSA. Fractions
664 containing >80% pachytene spermatocytes were identified by light microscopy, pooled, and
665 stored in cryoprotective media (DMEM supplemented with 10%FBS and 20%DMSO) at -80° C
666 pending further analysis.
667
668 Pachytene spermatocytes obtained were resuspended in RIPA buffer (50mM Tris-HCl pH 8.0,
669 150mM NaCl, 1% NP-40, 0.5% Sodium deoxycholate, 0.1% SDS, 5mM NaF, 1mM Na_3VO_4,
670 1mM Phenylmethylsulfonyl fluoride (PMSF), 1X Protease inhibitor cocktail (Sigma)) at 4˚C and
671 sonicated for 15 minutes followed by centrifugation at 12000xg for 10 minutes at 4˚C. Western
672 blotting was performed by separating samples in 5% SDS-polyacrylamide gel and transferring to
673 PVDF (polyvinylidene difluoride) membranes (Bio-Rad) overnight. Blots were scanned on a LI-
674 COR Odyssey CLx imager. Image Studio Version 5.2.5 was used to view blots and quantify
675 band intensity. Antibodies and their corresponding dilutions are listed (Supplementary Table 3).
676
677 **Flow cytometry**
678 To analyze isolated spermatocytes, the cells were resuspended in Hank's balanced salt solution
679 (HBSS) (10^6 cells/ml) at 4°C and stained with Live-or-Dye™ 615/740 fixable viability stain
680 (Biotium) for 30 minutes. After washing the cells 3 times with HBSS, they were fixed for 1 hour
681 and permeabilized using eBioscience™ Foxp3 / Transcription Factor Staining Buffer Set
682 (ThermoFisher). DNA was stained using Vybrant™ DyeCycle™ Violet Stain (ThermoFisher)
683 (1:1000) and analyzed by flow cytometry using LSRFortessa (BD Biosciences). FCS files were
684 obtained and analyzed using FlowJo software.
685
686 **RNA extraction and RT-PCR**
687 Total RNA was isolated in TRIzol™ reagent (Invitrogen, 15596026) from Sta-Put purified
688 fractions enriched for pachytene spermatocytes and round spermatids. The extracted RNA was
689 purified using the Direct-zol RNA kit (Zymo, R2050). cDNA was synthesized using a random
690 primer mix (New England Biolabs, S1330S) and ProtoScript® II reverse transcriptase (New

691 England Biolabs, M0368L). RT-PCR was performed on 1:10 cDNA dilutions using Sso Fast
692 EvaGreen supermix (Bio-Rad, 172-5280) on a thermocycler (BioRad, C1000). Amplicons
693 associated with either floxed or excised *Arid1a* cDNA's were detected using primers: (F)- 5' -
694 TCCAGTAAGGGAGGGCAAGAAGAT -3'; (R) 5' - GTAGTTGGCGTTGGGCAAGGCATTA -3'
695 (PCR product sizes- *fl*: 612 bp; *Δ*: 281 bp)
696
697 **RNA-seq**
698 RNA was extracted and purified in quadruplicate from frozen pellets of *Arid1a*^{WT} and *Arid1a*^{cKO}
699 pachytene spermatocytes obtained by Salmony Sta-Put gravity sedimentation using the
700 abovementioned methods. All samples displayed RNA integrity number (RIN) > 7.0 as
701 determined by Agilent Tapestation (High sensitivity RNA screen tape). Sequencing libraries
702 were prepared from 1 μg of total RNA using a Kapa mRNA HyperPrep kit (Roche, KK8580) per
703 the manufacturer's instruction. Libraries were quantified using Qubit™ dsDNA Hs assay kit
704 (Invitrogen, Q32854) pooled at equimolar concentrations, and sequenced on a single lane of the
705 Illumina NovaSeq 6000 S Prime flow cell (50 bp reads, paired-end).
706
707 **RNA-seq data analysis**
708 Gene expression was quantified using Salmon (Patro et al., 2017). Transcript counts at the
709 gene level were summarized using tximport (Soneson et al., 2016) and then imported to perform
710 a differential gene expression analysis using DESeq2 (Love et al., 2014). The mouse (mm10)
711 gene/transcript annotations were retrieved using AnotationDbi (Pàges et al., 2021) and
712 *TxDb.Mus musculus.UCSC.mm10.known gene (Bioconductor Core Team, 2019)* R packages
713 from Bioconductor. Low-count genes (< 10 reads) were pre-filtered, and significant differences
714 in counts were called at a false discovery rate (FDR)≤ 0.05. Supplementary Table 6 lists
715 differentially expressed genes.
716
717 **CUT&RUN (Cleavage Under Targets and Release Using Nuclease)**
718 CUT&RUN assays were performed on cryopreserved *Arid1a*^{WT} and *Arid1a*^{cKO} pachytene
719 spermatocytes (500,000 cells/genotype) obtained by Sta-Put, using a slightly modified version
720 of previously described methods (Meers et al., 2019; Skene and Henikoff, 2017). For ARID1A,
721 CUT&RUN was performed in triplicates per genotype with two different antibodies. H3.3
722 CUT&RUN was performed in duplicates on *Arid1a*^{WT} and triplicates on *Arid1a*^{cKO} samples.

723 Aliquots of cryopreserved *Arid1a*^{WT} and *Arid1a*^{cKO} pachytene spermatocytes were quickly
724 thawed in a water bath at room temperature (RT), pelleted at 600g for 5 minutes, and washed
725 [wash buffer: 20mM HEPES(Na) pH7.5, 150 mM NaCl, 0.5 mM spermidine, EDTA-free protease
726 inhibitor] three times. Cells were gently resuspended in wash buffer and bound to Concanavalin-
727 A coated magnetic beads (20 μL beads/500,000 cells) by mixing on a rotator for 15 minutes.
728 The bead slurry was separated using a magnet followed by permeabilization in 50 μL antibody
729 buffer (wash buffer + 0.05% Digitonin + 2mM EDTA) per sample in 0.2 mL 8-strip PCR tubes.
730 Primary antibody was added to the samples and incubated on a nutator at 4° C overnight. Cells
731 were then separated using a magnet, washed two times in 200 μL Dig-wash buffer (wash buffer
732 + 0.05% Digitonin), and incubated with a secondary antibody prepared in 50 μL of Dig-wash
733 buffer/sample for 30 minutes on a nutator at 4° C. After antibody incubations, samples were
734 washed twice in 200 μL Dig-wash buffer and then incubated on a nutator at 4° C with 50 μL Dig-
735 wash buffer containing 1000ng/mL Protein A/G Micrococcal Nuclease (pA/G-MNase) for 1 hr.
736 Following this, samples were washed twice in 200 μL Dig-wash buffer, resuspended in 50 μL
737 Dig-wash buffer, cooled down to 0° C, and supplemented with $CaCl_2$ at a final concentration of 2
738 mM to activate MNase. Samples were digested at 0 ^{o}C for 40 minutes. The resulting chromatin
739 fragments were extracted from the bead slurry by incubating in 2X STOP buffer (340 mM NaCl,
740 20mM EDTA, 4mM EGTA, 0.05% Digitonin, 100 μg/mL RNase A) at 37° C for 30 minutes. DNA
741 was purified using ChIP DNA clean and concentrator kit (Zymo, D5205). Libraries were
742 prepared using the Kapa Hyperprep kit (Roche, KK8504), examined for size, and quantified on
743 an Agilent 2100 bioanalyzer using the high-sensitivity DNA kit (Agilent, 5067-4626). The
744 libraries were pooled in equimolar amounts and sequenced on a single lane of the Illumina
745 NovaSeq 6000 S Prime flow cell (50 bp reads, paired-end). Antibody details are listed in
746 Supplementary Table 3. The pA/G-MNase (Addgene ID: 123461) used for the CUT&RUN
747 experiments was purified at UNC-Chapel Hill's Protein Expression and Purification core.
748
749 **CUT&RUN data analysis**
750 CUT&RUN data analyses were performed as previously described (Menon et al., 2021). Briefly,
751 fastq files were analyzed with fastqc (version 0.11.9), then processed with TrimGalore (version
752 0.6.2, https://www.bioinformatics.babraham.ac.uk/projects/trim_galore/) keeping the --trim-n
753 option. Trimmed reads were aligned to mm10 (mouse) reference genome using bowtie2
754 (Langmead and Salzberg, 2012) parameters: bowtie2 --very-sensitive-local --no-mixed --no-unal
755 --dovetail --no-discordant. Alignments were outputted in BAM format using samtools (Li et al.,

756 2009) and filtered for PCR duplicates using Picard tools, MarkDuplicates
757 (https://broadinstitute.github.io/picard/). Deduplicated BAM files were used to generate bigWig
758 files filtered for ENCODE mm10 blocked regions (Amemiya et al., 2019) with DeepTools,
759 bamCoverage (Ramírez et al., 2016) with the following options: -bs 30 --smoothLength 60 -bl --
760 scaleFactor. The option --scaleFactor was used to normalize for composition bias between
761 CUT&RUN libraries generated from *Arid1a*^{WT} and *Arid1a*^{cKO} pachytene spermatocytes.
762 csaw (Lun and Smyth, 2015) derived normalization factors (nf) were used to calculate the
763 effective library size (library size X nf). The inverse of the effective library size per million was
764 supplied to --scaleFactor to generate normalized bigWig files. Peak calling was performed with
765 MACS2 (version 2.1.2) with options: -f BAMPE --broad --broad-cutoff 0.05 --keep-dup all, on
766 filtered BAM files associated with ARID1A and H3.3 relative to an IgG control previously
767 generated from pachytene enriched populations obtained from P18 testes (Chakraborty and
768 Magnuson, 2022). Peak overlaps across replicates were determined using bedtools intersect
769 (Quinlan and Hall, 2010). Peak calls are provided in supplementary table 7. Peaks were
770 annotated using HOMER (version 4.9.1), annotatePeaks.pl. Replicate bigWig files were
771 averaged using WiggleTools (Zerbino et al., 2014). Averaged bigWig files generated heatmaps
772 with DeepTools, computeMatrix, and plotHeatmap. Data was visualized on Integrative
773 Genomics Viewer (Robinson et al., 2011).
774
775 **ATAC-seq**
776 Cryopreserved aliquots of *Arid1a*^{WT} and *Arid1a*^{cKO} pachytene spermatocytes were processed in
777 quadruplicate for ATAC-seq using the standard Omni-ATAC protocol (Corces et al., 2017) with
778 minor changes. These involved increasing the cell number to 100,000 per replicate, using
779 Diagenode tagmentase (loaded Tn5 transposase, C01070012) and Diagenode 2X tagmentation
780 buffer (C01019043). Libraries were quantified using NEBNext® kit for Illumina® (New England
781 Biolabs, E7630S), pooled at equimolar amounts, and sequenced on a single lane of the Illumina
782 NovaSeq 6000 S Prime flow cell (50 bp reads, paired end).
783
784 **ATAC-seq data analysis**
785 After analyzing the quality of fastq files with fastqc (version 0.11.9), they were processed with
786 TrimGalore (version 0.6.2), keeping the --trim-n option. Alignments to mm10 reference genome
787 were performed with bowtie2 (Langmead and Salzberg, 2012) parameters: bowtie2 --very-
788 sensitive -X 2000, and outputted in BAM format using samtools. Resultant BAM files were

filtered for PCR duplicates using Picard tools, MarkDuplicates, and mitochondrial reads using samtools view (code: samtools view -h Dedup.bam | grep -v 'chrM' | samtools view -b -h -f 0x2 - | samtools sort > Dedup_noChrM.bam). Filtered BAM files were used to call peaks with MACS2 (parameters: -f BAMPE -n de -q 0.05 --nomodel --nolambda --keep-dup all) and generate normalized bigWig files with DeepTools, bamCoverage (options: -bs 30 --smoothLength 60 -bl --normalized using RPKM). Peak overlaps across replicates were determined using bedtools intersect (Quinlan and Hall, 2010). Peak calls are provided in supplementary table 8. Peak annotation (annotatePeaks.pl) and motif analyses (findMotifsGenome.pl) were performed with HOMER (version 4.9.1). PRDM9 motif frequency near ATAC-seq peaks was determined using HOMER annotatePeaks.pl with options: -size 20000 -hist 10. Replicate bigWig files were averaged using WiggleTools (Zerbino et al., 2014). Averaged bigWig files generated heatmaps with DeepTools, computeMatrix, and plotHeatmap. Data was visualized on Integrative Genomics Viewer (Robinson et al., 2011).

DATA AVAILABILITY:

RNA-seq, CUT&RUN, and ATAC-seq data generated in this study are deposited with GEO (Gene Expression Omnibus) under accession number GSE225612. DMC1 SSDS (GSE35498), RAD51 SSDS (GSE143582), and H3K4me3 ChIP-seq (GSE89502) datasets were previously published (Brick et al., 2012; Hinch et al., 2020; Maezawa et al., 2018) and are available on GEO.

ACKNOWLEDGEMENTS

We thank Magnuson lab members for their helpful comments on manuscript preparation. Next-generation sequencing was performed at the Duke Center for Genomic and Computational Biology. pA/G-MNase was produced by the Protein Expression and Purification core at the University of North Carolina at Chapel Hill (supported by Cancer Center Support Grant, P30 CA16086). We thank Dr. Atilla Töth (Technishe Universität Dresden) for generously providing the HORMAD1 antibody. This work was supported by National Institutes of Health grants R01GM101974 (T.M).

AUTHOR CONTRIBUTIONS

D.U.M and T.M conceptualized and designed the project. D.U.M., PC, and N.M. carried out experiments. Data curation and validation are done by D.U.M, PC, and N.M. D.U.M, PC, and NM performed the writing, which was reviewed and edited by T.M. Project supervision and funding acquisition by T.M.

COMPETING INTERESTS

The authors declare no competing interests.

827 **Figure Legends**

828

829 **Fig 1. ARID1A associates with the sex body late in meiotic prophase-I.**

830 Representative wild-type pachytene and diplotene spermatocyte spreads immunolabelled for
831 ARID1A (magenta) and SYCP3 (green) and then counterstained for DNA (blue). Panel insets
832 denote a magnified view of the nuclear area surrounding the sex chromosomes. Scale bar:10
833 µm, magnification: 100x.

834

835 **Fig 2. Requirement of ARID1A for the repression of sex-linked genes.**

836 (A) MA plot describing the LOG2-fold-change (LFC, y-axis) in mean expression (x-axis) of
837 genes displaying significant (FDR≤0.05, magenta dots) changes in *Arid1a*^{cKO} relative to
838 *Arid1a*^{WT} pachytene spermatocytes. Dashed blue lines denote 2 LFC. Gray dots (FDR≥0.05)
839 depict non-significant changes in gene expression. (B) Violin plot describing the LOG2-fold-
840 change (LFC, y-axis) in the median chromosome-wide gene expression (x-axis) in *Arid1a*^{cKO}
841 relative to *Arid1a*^{WT} pachytene spermatocytes. The dashed blue line denotes no change in gene
842 expression.

843

844 **Fig 3. ARID1A limits RNA polymerase II (RNAPII) localization to the sex body.**

845 (A) *Arid1a*^{WT} and *Arid1a*^{cKO} pachytene spermatocytes immunolabelled for pSer2-RNAPII
846 (green), SYCP3 (cyan), and counterstained with DAPI (blue). Scale bar:15 µm, magnification:
847 100x. The sex chromosomes (white arrow) and sex body (yellow dashed circle) are labeled.
848 Brightness of the whole image panel (A) was increased by compressing the dynamic range of
849 the image panel using Adobe photoshop (0-1-255 to 0-1-150). (B) Dot plot describing the
850 corrected total pSer2-RNAPII fluorescence (y-axis) measured from *Arid1a*^{WT} (n = 82) and
851 *Arid1a*^{cKO} (n= 119) pachytene spermatocytes (3 replicates per genotype). Empty diamonds
852 (magenta) represent independent data points. Significance determined by a two-tailed unpaired
853 Student's t-test p values. Data expressed as mean (black dot) ± SEM.

854

855 **Fig 4. ARID1A limits promoter accessibility.**

856 (A) Genomic associations of MACS2 derived ATAC-seq peak calls from *Arid1a*^{WT} and *Arid1a*^{cKO}
857 pachytene spermatocytes. Percent (%) distribution of genomic annotations is indicated. (B-C)
858 Heatmap (bottom) and metaplot (top) displaying the average ATAC-seq signal associated with
859 differentially expressed (B) autosomal and (C) sex-linked genes in *Arid1a*^{WT} and *Arid1a*^{cKO}

860 pachytene spermatocytes. (B-C) The number of RefSeq annotations (n) associated with
861 differentially regulated genes (rows) is indicated. Up-reg: misexpressed, and Dn-reg:
862 misrepressed genes in response to the loss of ARID1A. Average ATAC-seq coverage was
863 plotted across RefSeq genes ± 3Kb.
864
865 **Fig 5. ARID1A influences the chromatin composition of the sex body.**
866 (A-B) *Arid1a*^{WT} and *Arid1a*^{cKO} pachytene spermatocytes immunolabelled for HORMAD1
867 (magenta), (A) ARID1A (cyan) and H3.3 (green), (B) ARID1A (green) and H3.1/3.2 (cyan). (A-B)
868 Proportion (%) of *Arid1a*^{WT} and *Arid1a*^{cKO} early, mid, and late pachytene spermatocytes
869 displaying distinct (A) H3.3, (B) H3.1/3.2 localization patterns with the sex body. For H3.3
870 immunostaining, the total number of *Arid1a*^{WT} pachytene spermatocytes: early = 144, mid= 274,
871 late= 95; *Arid1a*^{cKO} pachytene spermatocytes: early = 43, mid= 86, late= 55, were scored, from
872 3 replicates each. For H3.1/3.2 immunostaining, the total number of *Arid1a*^{WT} pachytene
873 spermatocytes: early = 91, mid= 124, late= 45; *Arid1a*^{cKO} pachytene spermatocytes: early = 22,
874 mid= 116, late= 58, were scored, from 3 replicates each. DNA counterstained with DAPI (blue).
875 The sex chromosomes (yellow arrow) and sex body (yellow dashed circle) are labeled. Scale
876 bar:15 µm, magnification: 100x. Brightness of the whole image panel (Fig. 5) was increased by
877 compressing the dynamic range of the image panels using Adobe photoshop (0-1-255 to 0-1-
878 150).
879
880 **Fig 6. H3.3 displays differential occupancy across ARID1A-governed sex-linked open**
881 **chromatin.**
882 (A-B) Heatmaps (bottom) and metaplots (top) displaying average (A) chromatin accessibility
883 (purple heatmap) and H3.3 enrichment (green heatmap) associated with lost, common, and
884 gained ATAC-seq peak calls (MACS2), (B) enrichment of H3.3 at k-means clusters associated
885 with common (C1-C4, left) and gained (G1-G4, right) ATAC-seq peaks, in *Arid1a*^{WT} and
886 *Arid1a*^{cKO} pachytene spermatocytes. (A-B) ATAC-seq and H3.3 coverage plotted over a 5 Kb
887 window centered at ATAC-seq peaks (MACS2). Number of ATAC-seq peak calls (n) associated
888 with each category is indicated.
889
890 **Fig 7. ARID1A influences the axial association of DMC1 with the XY during pachynema.**
891 (A) *Arid1a*^{WT} and *Arid1a*^{cKO} pachytene spermatocytes immunolabelled for HORMAD1
892 (magenta), ARID1A (green), DMC1 (cyan), and counterstained with DAPI (blue). Scale bar:15

893 µm, magnification: 100x. A magnified view of the sex chromosomes is indicated (yellow dashed
894 square). (B) Dot plot displaying the number of sex-linked DMC1 foci (y-axis) quantified from
895 *Arid1a*^{WT} (n = 66) and *Arid1a*^{cKO} (ARID1A^{-}, n= 75) pachytene spermatocytes, obtained from 3
896 replicates each. Empty diamonds (magenta) represent independent data points. Significance
897 determined using a two-tailed unpaired Student's t-test p values. Data expressed as mean
898 (black dot) ± SEM.
899
900 **Fig 8. A model describing the role of ARID1A sex-linked chromatin regulation.**
901 During meiosis, the sex chromosomes undergo transcriptional repression at the onset of
902 pachynema. A dramatic change in the composition of sex-linked chromatin accompanies this
903 chromosome-wide repression. From mid to late pachynema, spermatocytes display a hyper-
904 accumulation of the variant histone H3.3 (Ochre shading and gradient) on the sex
905 chromosomes (magenta) relative to autosomes (green). Concomitantly, the canonical histones
906 H3.1/3.2 levels and elongating pSer2-RNAPII complex (grey gradients) appear depleted from
907 the sex body by late pachynema. The loss of ARID1A dramatically alters the chromatin
908 composition of the sex body, which features low H3.3 (yellow bar) association at levels
909 indistinguishable from autosomes throughout pachynema. Concomitantly, canonical H3.1/3.2
910 and pSer2-RNAPII levels (grey bar) on the sex body remain abnormally stable throughout
911 pachynema. These sex-linked chromatin aberrations, along with persistent transcription owing
912 to the association of pSer2-RNAPII with mutant sex body, fail meiotic sex chromosome
913 inactivation (MSCI) and, consequently, pachytene arrest. This defect also coincides with an
914 abnormal loss of DMC1 (blue foci) localization to the unpaired sex chromatids in response to the
915 loss of ARID1A. Therefore, along with transcriptional repression, ARID1A-governed chromatin
916 dynamics appear to influence DNA repair on the sex chromosomes.
917
918 **Table 1. The loss of ARID1A results in a pachytene arrest.**
919 Table outlining the distribution of P23 *Arid1a*^{WT} and *Arid1a*^{cKO} meiotic prophase-I profiles.
920 SYCP3 staining determined meiotic staging. Co-staining of ARID1A identified mutant
921 spermatocytes from escaper. The total number of spermatocytes scored included 166 for
922 *Arida*$^{fl/fl}$ and 124 for *Arid1a*^{cKO}. * denotes *Arid1a*^{cKO} diplotene spermatocytes with partially
923 reduced but not complete loss of ARID1A signal relative to controls.
924
925 **Fig S1. ARID1A transcripts detected in pachytene spermatocytes.**

926 scRNA-seq profiles of *Arid1a* and *Arid1b* in adult testes from B6 mice (Ernst et al., 2019). (A)
927 tSNE plot describing the clustering of various spermatogenic stages. LOG2 normalized
928 expression counts of (B,C) *Arid1a* and (D,E) *Arid1b* represented by tSNE plots and bar plots.
929 (B,D) tSNE plots illustrating the first (tSNE1, x-axis) and second dimensions (tSNE2, y-axis) .
930 (C,E) Bar plots describe the gene's mRNA abundance (y-axis) across identified germ cell
931 clusters (x-axis). (A) eP: early pachynema, mP: mid pachynema, lP: late pachynema, MI:
932 Metaphase-I, MII: Metaphase-II, S1-S11: Spermatid stages. Plots generated with shiny app
933 (https://marionilab.cruk.cam.ac.uk/SpermatoShiny)
934
935 **Fig S2. Western blot for ARID1A** in wild-type and mutant pachytene spermatocytes (left) and
936 with quantitation (right). The Uniprot entry for Mouse ARID1A only indicates a large mol.wt
937 sequence of ~242 kDa. There is no evidence to suggest that lower molecular weight isoforms
938 may be translated. Although speculative, it is possible that the lower molecular weight bands
939 represent proteolytic/proteasomal degradation products or products of antibody non-specificity.
940 Nucleolin (NCL) is the loading control. Bars in B represent mean ± S.E.M. *; $p<0.01$. The
941 antibody used for the Western blot is a rabbit anti-ARID1A (D2A8U from Cell Signaling
942 Technology 12354).
943
944 **Fig S3. Spermatogenesis appears unperturbed in *Arid1a^{cKO}* males.**
945 Histological examination of (A) PAS-stained seminiferous tubule sections and (B) H&E-stained
946 cauda epididymal sections obtained from adult *Arid1a^{WT} and Arid1a^{cKO}* mice. The micrograph
947 depicts seminiferous tubule staging and scale bars (50 µm). Magnification: 40x.
948
949 **Fig S4. *Arid1a^{cKO}* testes display inefficient *Stra8-Cre* activity.**
950 (A) Schematic (top) illustrating the region of *Arid1a^{fl}* allele spanning exons (ex) 4-8 (grey boxes)
951 along with the location of *loxP* sites (solid magenta arrowheads) and primer annealing sites
952 (blue arrows). (A bottom): analysis of the RT-PCR of *Arid1a* transcripts from STA-PUT purified
953 populations of *Arid1a^{WT} and Arid1a^{cKO}* pachytene spermatocytes (left) and round spermatids
954 (right). DNA electrophoresis gels indicate bands corresponding to the fl: floxed and Δ: excised
955 PCR products. *Arid1a^{WT}* and *Arid1a^{cKO}* (B) testes cryosections and (C) spermatocyte spreads,
956 immunolabelled for ARID1A (magenta), SYCP3 (green), and counterstained for DNA (blue). (B)
957 Scale bar: 20 µm, magnification: 63x, P: Pachytene, D: Diplotene, and M-I: Metaphase-I

958 spermatocytes. (C) Scale bar:15 µm, magnification: 100x. Brightness of the whole panels (B,C)
959 were increased by compressing the dynamic range of the image panels using Adobe photoshop
960 (0-1-255 to 0-1-150).
961
962 **Fig S5. Arid1a mutant testes exhibit aberrant meiotic prophase I, reducing the abundance**
963 **of round spermatids during the first wave of spermatogenesis.**
964 (A) The abundance of round spermatids on P26 was determined by measuring the 1C DNA
965 content through DNA staining and flow cytometry. (B) Bars represent the quantification of round
966 spermatids (mean ± S.E.M.). *; $p<0.01$ (n=3)
967
968 **Fig S6. Transcription start sites of differentially expressed autosomal and sex-linked**
969 **genes display ARID1A occupancy.**
970 (A-B) Heatmap (bottom) and metaplot (top) displaying the average gene-wide enrichment of
971 ARID1A associated with differentially expressed (A) autosomal and (B) sex-linked genes in
972 *Arid1a*^{WT} and *Arid1a*^{cKO} pachytene spermatocytes. (A-B) The number of RefSeq annotations (n)
973 associated with differentially regulated autosomal and sex-linked genes (rows) is indicated. Up-
974 reg: misexpressed and Dn-reg: misrepressed genes in response to the loss of ARID1A.
975 Average ARID1A CUT&RUN coverage was determined using two antibodies (anti-ARID1A^{Sigma};
976 anti-ARID1A^{CST}) plotted across RefSeq genes ± 3Kb.
977
978 **Fig S7. ARID1A does not influence sex body formation.**
979 (A) *Arid1a*^{WT} and *Arid1a*^{cKO} spermatocyte spreads immunolabelled for ARID1A (magenta) and
980 γH2Ax (green). Scale bar:15 µm, magnification: 100x. (B) Cross section of adult (3-month-old)
981 *Arid1a*^{WT} and *Arid1a*^{cKO} seminiferous tubules immunolabelled for ARID1A (green) and ATR
982 (cyan). Scale bar:15 µm, magnification: 63x. (C) *Arid1a*^{WT} and *Arid1a*^{cKO} pachytene
983 spermatocytes immunolabelled for MDC1 (magenta), SYCP3 (cyan), and ARID1A (green).
984 Scale bar:15 µm, magnification: 100x. (A-B) DNA counterstained with DAPI (blue). Brightness of
985 the whole image panel (C) was increased by compressing the dynamic range of the image
986 panel using Adobe photoshop (0-1-255 to 0-1-150).
987
988 **Fig S8. ARID1A does not influence the expression or incorporation of H3.3.**
989 (A) Western blots on acid-extracted histones obtained from four independent replicates of P19
990 *Arid1a*^{WT} and *Arid1a*^{cKO} spermatogenic cells, displaying H3.3 abundance. Total histone levels

991 from each sample are displayed. (B) *Arid1a*^{WT} and *Arid1a*^{cKO} pachytene spermatocytes
992 immunolabelled for HORMAD1 (magenta), DAXX (cyan), and ARID1A (green). DNA
993 counterstained with DAPI (blue). The sex chromosomes (yellow arrow) and sex body (yellow
994 dashed circle) are labeled. Scale bar:15 µm, magnification: 100x. (C) *Arid1a*^{WT} and *Arid1a*^{cKO}
995 testis cryosections immunolabelled for ARID1A (magenta) and HIRA (green). DNA
996 counterstained with DAPI (blue). Representative mutant (white arrows) and escaper (yellow
997 arrows) pachytene spermatocytes labeled in *Arid1a*^{cKO} testis cryosection. Scale bar: 15 µm,
998 magnification: 63x. Brightness of the whole panels (B,C) were increased by compressing the
999 dynamic range of the image panels using Adobe photoshop (0-1-255 to 0-1-150).
1000
1001 **Fig S9. ARID1A limits H3.3 occupancy at promoters**
1002 (A) Genomic associations of MACS2 H3.3 peak calls from *Arid1a*^{WT} and *Arid1a*^{cKO} pachytene
1003 spermatocytes. Percent (%) distribution of genomic annotations is indicated. (B-C) Heatmap
1004 (bottom) and metaplot (top) displaying the average H3.3 signal associated with differentially
1005 expressed (B) autosomal and (C) sex-linked genes in *Arid1a*^{WT} and *Arid1a*^{cKO} pachytene
1006 spermatocytes. (B-C) The number of RefSeq annotations (n) associated with differentially
1007 regulated genes (rows) is indicated. Up-reg: misexpressed, and Dn-reg: misrepressed genes in
1008 response to the loss of ARID1A. Average H3.3 coverage plotted across RefSeq genes ± 3Kb.
1009
1010 **Fig S10. Genome browser views of ARID1A governed H3.3 genomic associations.**
1011 H3.3 CUT&RUN coverage from *Arid1a*^{WT} (green tracks) and *Arid1a*^{cKO} (Orange tracks)
1012 pachytene spermatocytes. Solid red bars and yellow highlights denote H3.3 peak calls (MACS2)
1013 from *Arid1a*^{WT} and *Arid1a*^{cKO} pachytene spermatocytes. Vertical viewing limits within
1014 parentheses.
1015
1016 **Fig S11. H3.3 occupancy is antagonistic to DMC1 associations in non-homologous sex-**
1017 **linked regions.**
1018 (A) Genomic associations of common (C1-C4) and gained (G1-G4) k-means clusters in
1019 pachytene spermatocytes. Percent (%) distribution of genomic annotations is indicated. (B)
1020 Results of PRDM9 motif enrichment analyses at gained (G1 and G3), k-means clusters (top),
1021 and plots describing the frequency of PRDM9 motifs (y-axis) spanning a 5 Kb window centered
1022 at ATAC-seq peaks (x-axis) associated with gained (middle) and common (bottom) k-means
1023 clusters that are either deficient (orange trend line) or enriched (cyan trend line) for H3.3

1024 occupancy. Trend lines were generated using generalized additive mode smoothing (gam). 95%
1025 confidence interval (gray shading) is indicated. (C-D) Heatmaps displaying testes DMC1 (left)
1026 and pachytene spermatocyte associated H3K4me3 (right) enrichment relative to input at k-
1027 means clusters associated with (C) gained (G1-G4), and (D) common (C1-C4) ATAC-seq
1028 peaks. (C-D) DMC1 and H3K4me3 coverage plotted over a 10 Kb window centered at ATAC-
1029 seq peaks (MACS2).
1030
1031 **Fig S12. ARID1A does not affect the axial association of RAD51 with the XY during**
1032 **pachynema.**
1033 (A) Heatmaps displaying testes RAD51 enrichment relative to input at k-means clusters
1034 associated with gained (G1-G4, left) and common (C1-C4, right) ATAC-seq peaks. RAD51
1035 coverage plotted over a 10 Kb window centered at ATAC-seq peaks (MACS2). (B) *Arid1a*^{WT} and
1036 *Arid1a*^{cKO} pachytene spermatocytes immunolabelled for HORMAD1 (magenta), RAD51 (green)
1037 and counterstained with DAPI (blue). Scale bar:15 µm, magnification: 100x. Yellow arrows and
1038 dashed circles label the sex chromosomes.
1039
1040 **Table S1.** There is no significant difference in the numbers of undifferentiated spermatogonia
1041 expressing PLZF in 1-month-old *Arid1a*^{cKO} relative to *Arid1a*$^{fl/fl}$ males.
1042

1043 **References**

1044 **Ahmed, E. A. and de Rooij, D. G.** (2009). Staging of Mouse Seminiferous Tubule Cross-Sections.
1045 In *Meiosis* (ed. Keeney, S.), pp. 263–277. Totowa, NJ: Humana Press.

1046 **Alavattam, K. G., Maezawa, S., Andreassen, P. R. and Namekawa, S. H.** (2022). Meiotic sex
1047 chromosome inactivation and the XY body: a phase separation hypothesis. *Cell. Mol. Life*
1048 *Sci.* **79**, 18.

1049 **Alexander, A. K., Rice, E. J., Lujic, J., Simon, L. E., Tanis, S., Barshad, G., Zhu, L., Lama, J.,**
1050 **Cohen, P. E. and Danko, C. G.** (2023). A-MYB and BRDT-dependent RNA Polymerase II
1051 pause release orchestrates transcriptional regulation in mammalian meiosis. *Nat.*
1052 *Commun.* **14**, 1753.

1053 **Amemiya, H. M., Kundaje, A. and Boyle, A. P.** (2019). The ENCODE Blacklist: Identification of
1054 Problematic Regions of the Genome. *Sci. Rep.* **9**, 9354.

1055 **Baarends, W. M., Wassenaar, E., van der Laan, R., Hoogerbrugge, J., Sleddens-Linkels, E.,**
1056 **Hoeijmakers, J. H. J., de Boer, P. and Grootegoed, J. A.** (2005). Silencing of Unpaired
1057 Chromatin and Histone H2A Ubiquitination in Mammalian Meiosis. *Mol. Cell Biol.* **25**,
1058 1041–1053.

1059 **Bellvé, A. R.** (1993). [6] Purification, culture, and fractionation of spermatogenic cells. In
1060 *Methods Enzymol.*, pp. 84–113. Elsevier.

1061 **Bioconductor Core Team** (2019). TxDb.Mmusculus.UCSC.mm10.knownGene: Annotation
1062 package for TxDb object(s).

1063 **Brick, K., Smagulova, F., Khil, P., Camerini-Otero, R. D. and Petukhova, G. V.** (2012a). Genetic
1064 recombination is directed away from functional genomic elements in mice. *Nature* **485**,
1065 642–645.

1066 **Chakraborty, P. and Magnuson, T.** (2022). INO80 requires a polycomb subunit to regulate the
1067 establishment of poised chromatin in murine spermatocytes. *Development* **149**,
1068 dev200089.

1069 **Chandler, R. L., Damrauer, J. S., Raab, J. R., Schisler, J. C., Wilkerson, M. D., Didion, J. P.,**
1070 **Starmer, J., Serber, D., Yee, D., Xiong, J., et al.** (2015). Coexistent ARID1A–PIK3CA
1071 mutations promote ovarian clear-cell tumorigenesis through pro-tumorigenic
1072 inflammatory cytokine signalling. *Nat. Commun.* **6**, 6118.

1073 **Chaumeil, J., Le Baccon, P., Wutz, A. and Heard, E.** (2006). A novel role for Xist RNA in the
1074 formation of a repressive nuclear compartment into which genes are recruited when
1075 silenced. *Genes Dev.* **20**, 2223–2237.

1076 **Clapier, C. R., Iwasa, J., Cairns, B. R. and Peterson, C. L.** (2017). Mechanisms of action and
1077 regulation of ATP-dependent chromatin-remodelling complexes. *Nat*. *Rev. Mol. Cell Biol*.
1078 **18,** 407-422.

1079 **Corces, M. R., Trevino, A. E., Hamilton, E. G., Greenside, P. G., Sinnott-Armstrong, N. A.,**
1080 **Vesuna, S., Satpathy, A. T., Rubin, A. J., Montine, K. S., Wu, B., et al.** (2017). An
1081 improved ATAC-seq protocol reduces background and enables interrogation of frozen
1082 tissues. *Nat Methods* **14**, 959–962.

1083 **Ellnati, E., Russell, H. R., Ojarikre, O. A., Sangrithi, M., Hirota, T., de Rooij, D. G., McKinnon, P.**
1084 **J. and Turner, J. M. A.** (2017). DNA damage response protein TOPBP1 regulates X
1085 chromosome silencing in the mammalian germ line. *Proc. Natl. Acad. Sci. U.S.A.* **114**,
1086 12536–12541.

1087 **Ernst, C., Eling, N., Martinez-Jimenez, C. P., Marioni, J. C. and Odom, D. T.** (2019). Staged
1088 developmental mapping and X chromosome transcriptional dynamics during mouse
1089 spermatogenesis. *Nat Commun.* **10**, 1251.

1090 **Fernandez-Capetillo, O., Mahadevaiah, S. K., Celeste, A., Romanienko, P. J., Camerini-Otero,**
1091 **R. D., Bonner, W. M., Manova, K., Burgoyne, P. and Nussenzweig, A.** (2003). H2AX Is
1092 Required for Chromatin Remodeling and Inactivation of Sex Chromosomes in Male
1093 Mouse Meiosis. *Dev. Cell* **4**, 497–508.

1094 **Fontaine, E., Papin, C., Martinez, G., Le Gras, S., Nahed, R. A., Héry, P., Buchou, T., Ouararhni,**
1095 **K., Favier, B., Gautier, T., et al.** (2022). Dual role of histone variant H3.3B in
1096 spermatogenesis: positive regulation of piRNA transcription and implication in X-
1097 chromosome inactivation. *Nucleic Acids Res* **50**, 7350–7366.

1098 **Gray, S., Santiago, E. R., Chappie, J. S. and Cohen, P. E.** (2020). Cyclin N-Terminal Domain-
1099 Containing-1 Coordinates Meiotic Crossover Formation with Cell-Cycle Progression in a
1100 Cyclin-Independent Manner. *Cell Rep* **32**, 107858.

1101 **Handel, M.** (2004). The XY body: a specialized meiotic chromatin domain. *Exp. Cell Res.* **296**,
1102 57–63.

1103 **Hasegawa, K., Sin, H.-S., Maezawa, S., Broering, T. J., Kartashov, A. V., Alavattam, K. G.,**
1104 **Ichijima, Y., Zhang, F., Bacon, W. C., Greis, K. D., et al.** (2015). SCML2 establishes the
1105 male germline epigenome through regulation of histone H2A ubiquitination. *Dev. Cell*
1106 **32**, 574–588.

1107 **Hinch, A. G., Becker, P. W., Li, T., Moralli, D., Zhang, G., Bycroft, C., Green, C., Keeney, S., Shi,**
1108 **Q., Davies, B., et al.** (2020). The Configuration of RPA, RAD51, and DMC1 Binding in
1109 Meiosis Reveals the Nature of Critical Recombination Intermediates. *Mol. Cell* **79**, 689-
1110 701.e10.

1111 **Hirota, T., Blakeley, P., Sangrithi, M. N., Mahadevaiah, S. K., Encheva, V., Snijders, A. P.,**
1112 **Ellnati, E., Ojarikre, O. A., de Rooij, D. G., Niakan, K. K., et al.** (2018). SETDB1 Links the
1113 Meiotic DNA Damage Response to Sex Chromosome Silencing in Mice. *Dev. Cell* **47**, 645-
1114 659.e6.

1115 **Ichijima, Y., Ichijima, M., Lou, Z., Nussenzweig, A., Camerini-Otero, R. D., Chen, J.,**
1116 **Andreassen, P. R. and Namekawa, S. H.** (2011). MDC1 directs chromosome-wide
1117 silencing of the sex chromosomes in male germ cells. *Genes Dev.* **25**, 959–971.

1118 **Keniry, A., Jansz, N., Gearing, L. J., Wanigasuriya, I., Chen, J., Nefzger, C. M., Hickey, P. F.,**
1119 **Gouil, Q., Liu, J., Breslin, K. A., et al.** (2022). BAF complex-mediated chromatin
1120 relaxation is required for establishment of X chromosome inactivation. *Nat. Comm.* **13**,
1121 1658.

1122 **Khalil, A. M., Boyar, F. Z. and Driscoll, D. J.** (2004). Dynamic histone modifications mark sex
1123 chromosome inactivation and reactivation during mammalian spermatogenesis. *Proc*
1124 *Natl Acad Sci U S A* **101**, 16583–16587.

1125 **Kim, Y., Fedoriw, A. M. and Magnuson, T.** (2012). An essential role for a mammalian SWI/SNF
1126 chromatin-remodeling complex during male meiosis. *Development* **139**, 1133–1140.

1127 **Langmead, B. and Salzberg, S. L.** (2012). Fast gapped-read alignment with Bowtie 2. *Nat.*
1128 *Methods* **9**, 357–359.

1129 **Li, H., Handsaker, B., Wysoker, A., Fennell, T., Ruan, J., Homer, N., Marth, G., Abecasis, G. and**
1130 **Durbin, R.** (2009). The Sequence Alignment/Map format and SAMtools. *Bioinformatics*
1131 **25**, 2078–2079.

1132 **Love, M. I., Huber, W. and Anders, S.** (2014). Moderated estimation of fold change and
1133 dispersion for RNA-seq data with DESeq2. *Genome Biol* **15**, 550.

1134 **Lun, A. T. L. and Smyth, G. K.** (2015). Csaw: A Bioconductor package for differential binding
1135 analysis of ChIP-seq data using sliding windows. *Nucleic Acids Res.* **44**, 1–10.

1136 **Maezawa, S., Hasegawa, K., Yukawa, M., Kubo, N., Sakashita, A., Alavattam, K. G., Sin, H.-S.,**
1137 **Kartashov, A. V., Sasaki, H., Barski, A., et al.** (2018a). Polycomb protein SCML2
1138 facilitates H3K27me3 to establish bivalent domains in the male germline. *Proc. Natl.*
1139 *Acad. Sci. U.S.A.* **115**, 4957–4962.

1140 **Maezawa, S., Yukawa, M., Alavattam, K. G., Barski, A. and Namekawa, S. H.** (2018b). Dynamic
1141 reorganization of open chromatin underlies diverse transcriptomes during
1142 spermatogenesis. *Nucleic Acids Res* **46**, 593–608.

1143 **Manterola, M., Brown, T. M., Oh, M. Y., Garyn, C., Gonzalez, B. J. and Wolgemuth, D. J.**
1144 (2018). BRDT is an essential epigenetic regulator for proper chromatin organization,

1145 silencing of sex chromosomes and crossover formation in male meiosis. *PLoS Genet* **14**,
1146 e1007209.

1147 **Meers, M. P., Bryson, T. D., Henikoff, J. G. and Henikoff, S.** (2019). Improved CUT&RUN
1148 chromatin profiling tools. *eLife* **8**, e46314.

1149 **Meistrich, M. L. and Hess, R. A.** (2013). Assessment of Spermatogenesis Through Staging of
1150 Seminiferous Tubules. In *Spermatogenesis* (ed. Carrell, D. T.) and Aston, K. I.), pp. 299–
1151 307. Totowa, NJ: Humana Press.

1152 **Menon, D. U., Shibata, Y., Mu, W. and Magnuson, T.** (2019). Mammalian SWI/SNF collaborates
1153 with a polycomb-associated protein to regulate male germ line transcription in the
1154 mouse. *Development* **146**, dev174094.

1155 **Menon, D. U., Kirsanov, O., Geyer, C. B. and Magnuson, T.** (2021). Mammalian SWI/SNF
1156 chromatin remodeler is essential for reductional meiosis in males. *Nat Commun* **12**,
1157 6581.

1158 **Moens, P. B., Chen, D. J., Shen, Z., Kolas, N., Tarsounas, M., Heng, H. H. Q. and Spyropoulos,**
1159 **B.** (1997). Rad51 immunocytology in rat and mouse spermatocytes and oocytes.
1160 *Chromosoma* **106**, 207–215.

1161 **Moens, P. B., Kolas, N. K., Tarsounas, M., Marcon, E., Cohen, P. E. and Spyropoulos, B.** (2002).
1162 The time course and chromosomal localization of recombination-related proteins at
1163 meiosis in the mouse are compatible with models that can resolve the early DNA-DNA
1164 interactions without reciprocal recombination. *J Cell Sci* **115**, 1611–1622.

1165 **Monesi, V.** (1964). Ribonucleic acid synthesis during mitosis and meiosis in the mouse testis. *J.*
1166 *Cell Biol.* **22**, 521–532.

1167 **Noe Gonzalez, M., Blears, D. and Svejstrup, J. Q.** (2021). Causes and consequences of RNA
1168 polymerase II stalling during transcript elongation. *Nat Rev Mol Cell Biol* **22**, 3–21.

1169 **O'Brien, D.** (1993). Isolation, separation, and short-term culture of spermatogenic cells. In
1170 *Methods in Toxicology*, pp. 246–264. San Diego: Academic Press.

1171 **Pàges, H., Carlson, M., Falcon, S. and Nianhua, L.** (2021). AnnotationDbi: Manipulation of
1172 SQLite-based annotations in Bioconductor. *R package version 1.562.2*.

1173 **Patro, R., Duggal, G., Love, M. I., Irizarry, R. A. and Kingsford, C.** (2017). Salmon provides fast
1174 and bias-aware quantification of transcript expression. *Nat Methods* **14**, 417–419.

1175 **Quinlan, A. R. and Hall, I. M.** (2010). BEDTools: A flexible suite of utilities for comparing
1176 genomic features. *Bioinformatics* **26**, 841–842.

1177 **Ramírez, F., Ryan, D. P., Grüning, B., Bhardwaj, V., Kilpert, F., Richter, A. S., Heyne, S., Dündar,**
1178 **F. and Manke, T.** (2016). deepTools2: a next generation web server for deep-sequencing
1179 data analysis. *Nucleic Acids Res* **44**, W160–W165.

1180 **Reske, J. J., Wilson, M. R., Armistead, B., Harkins, S., Perez, C., Hrit, J., Adams, M., Rothbart, S.**
1181 **B., Missmer, S. A., Fazleabas, A. T., et al.** (2022). ARID1A-dependent maintenance of
1182 H3.3 is required for repressive CHD4-ZMYND8 chromatin interactions at super-
1183 enhancers. *BMC Biol.* **20**, 209.

1184 **Robinson, J. T., Thorvaldsdóttir, H., Winckler, W., Guttman, M., Lander, E. S., Getz, G. and**
1185 **Mesirov, J. P.** (2011). Integrative genomics viewer. *Nat Biotechnol* **29**, 24–26.

1186 **Rogers, R. S., Inselman, A., Handel, M. A. and Matunis, M. J.** (2004). SUMO modified proteins
1187 localize to the XY body of pachytene spermatocytes. *Chromosoma* **113**, 233–243.

1188 **Royo, H., Prosser, H., Ruzankina, Y., Mahadevaiah, S. K., Cloutier, J. M., Baumann, M.,**
1189 **Fukuda, T., Höög, C., Tóth, A., de Rooij, D. G., et al.** (2013). ATR acts stage specifically to
1190 regulate multiple aspects of mammalian meiotic silencing. *Genes Dev.* **27**, 1484–1494.

1191 **Sadate-Ngatchou, P. I., Payne, C. J., Dearth, A. T. and Braun, R. E.** (2008). Cre recombinase
1192 activity specific to postnatal, premeiotic male germ cells in transgenic mice. *Genesis* **46**,
1193 738–742.

1194 **Schimenti, J.** (2005). Synapsis or silence. *Nat Genet* **37**, 11–13.

1195 **Schindelin, J., Arganda-Carreras, I., Frise, E., Kaynig, V., Longair, M., Pietzsch, T., Preibisch, S.,**
1196 **Rueden, C., Saalfeld, S., Schmid, B., et al.** (2012). Fiji: An open-source platform for
1197 biological-image analysis. *Nature Methods* **9** 676-682.

1198 **Shechter, D., Dormann, H. L., Allis, C. D. and Hake, S. B.** (2007). Extraction, purification and
1199 analysis of histones. *Nat. Protoc.* **2**, 1445–1457.

1200 **Skene, P. J. and Henikoff, S.** (2017). An efficient targeted nuclease strategy for high-resolution
1201 mapping of DNA binding sites. *eLife* **6**, e21856.

1202 **Soneson, C., Love, M. I. and Robinson, M. D.** (2016). Differential analyses for RNA-seq:
1203 transcript-level estimates improve gene-level inferences. *F1000Research* **4**, 1521.

1204 **Turner, J. M. A.** (2007). Meiotic sex chromosome inactivation. *Development* **134**, 1823–1831.

1205 **Turner, J. M. A., Aprelikova, O., Xu, X., Wang, R., Kim, S., Chandramouli, G. V. R., Barrett, J. C.,**
1206 **Burgoyne, P. S. and Deng, C. X.** (2004). BRCA1, histone H2AX phosphorylation, and male
1207 meiotic sex chromosome inactivation. *Curr. Biol.* **14**, 2135–2142.

1208 **Turner, J. M. A., Mahadevaiah, S. K., Fernandez-Capetillo, O., Nussenzweig, A., Xu, X., Deng,**
1209 **C.-X. and Burgoyne, P. S.** (2005). Silencing of unsynapsed meiotic chromosomes in the
1210 mouse. *Nat Genet* **37**, 41–47.

1211 **van der Heijden, G. W., Derijck, A. A. H. A., Pósfai, E., Giele, M., Pelczar, P., Ramos, L.,**
1212 **Wansink, D. G., van der Vlag, J., Peters, A. H. F. M. and de Boer, P.** (2007).
1213 Chromosome-wide nucleosome replacement and H3.3 incorporation during mammalian
1214 meiotic sex chromosome inactivation. *Nat Genet* **39**, 251–258.

1215 **Wang, J., Gu, H., Lin, H. and Chi, T.** (2012). Essential roles of the chromatin remodeling factor
1216 BRG1 in spermatogenesis in mice. *Biol. Reprod.* **86**, 186.

1217 **Wen, H., Li, Y., Xi, Y., Jiang, S., Stratton, S., Peng, D., Tanaka, K., Ren, Y., Xia, Z., Wu, J., et al.**
1218 (2014). ZMYND11 links histone H3.3K36me3 to transcription elongation and tumour
1219 suppression. *Nature* **508**, 263–268.

1220 **Yuen, B. T. K., Bush, K. M., Barrilleaux, B. L., Cotterman, R. and Knoepfler, P. S.** (2014). Histone
1221 H3.3 regulates dynamic chromatin states during spermatogenesis. *Development* **141**,
1222 3483–3494.

1223 **Zerbino, D. R., Johnson, N., Juettemann, T., Wilder, S. P. and Flicek, P.** (2014). WiggleTools:
1224 Parallel processing of large collections of genome-wide datasets for visualization and
1225 statistical analysis. *Bioinformatics **30**, 1008-1009.*.

1226 **Zhang, Y., Liu, T., Meyer, C. A., Eeckhoute, J., Johnson, D. S., Bernstein, B. E., Nussbaum, C.,**
1227 **Myers, R. M., Brown, M., Li, W., et al.** (2008). Model-based analysis of ChIP-Seq
1228 (MACS). *Genome Biology* **9**, R137.

1229

Meiotic Profile (P23)	*Arid1a*$^{fl/fl}$ (n= 166)	*Arid1a*^{cKO} (n= 124)
Pre-Lep/Leptonema	3.6 %	13.7 %
Zygonema	-	15.3 %
Early Pachynema	13.8 %	12.9 %
Mid Pachynema	22.89 %	40.3 %
late Pachynema	7.22 %	7.2 %
Early Diplonema	38.5 %	4.8 % *
Late Diplonema	14.45 %	5.6 % *

Table 1. The loss of ARID1A results in a pachytene arrest.

1

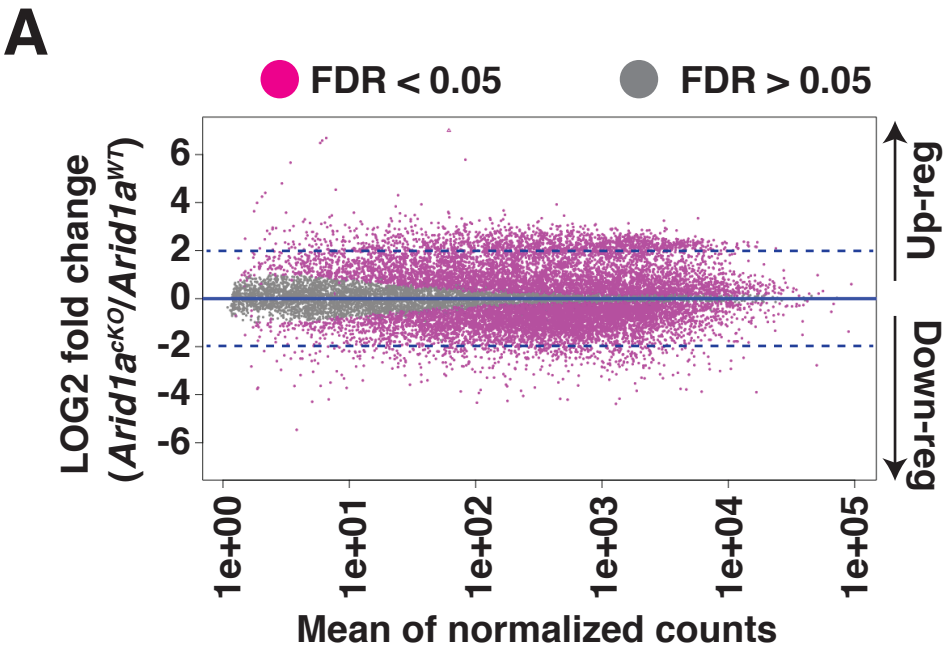
A
FDR < 0.05
FDR > 0.05
LOG2 fold change
(Arid1a^cKO/Arid1a^WT)
6
4
2
0
-2
-4
-6
Up-reg
Down-reg
1e+00
1e+01
1e+02
1e+03
1e+04
1e+05
Mean of normalized counts

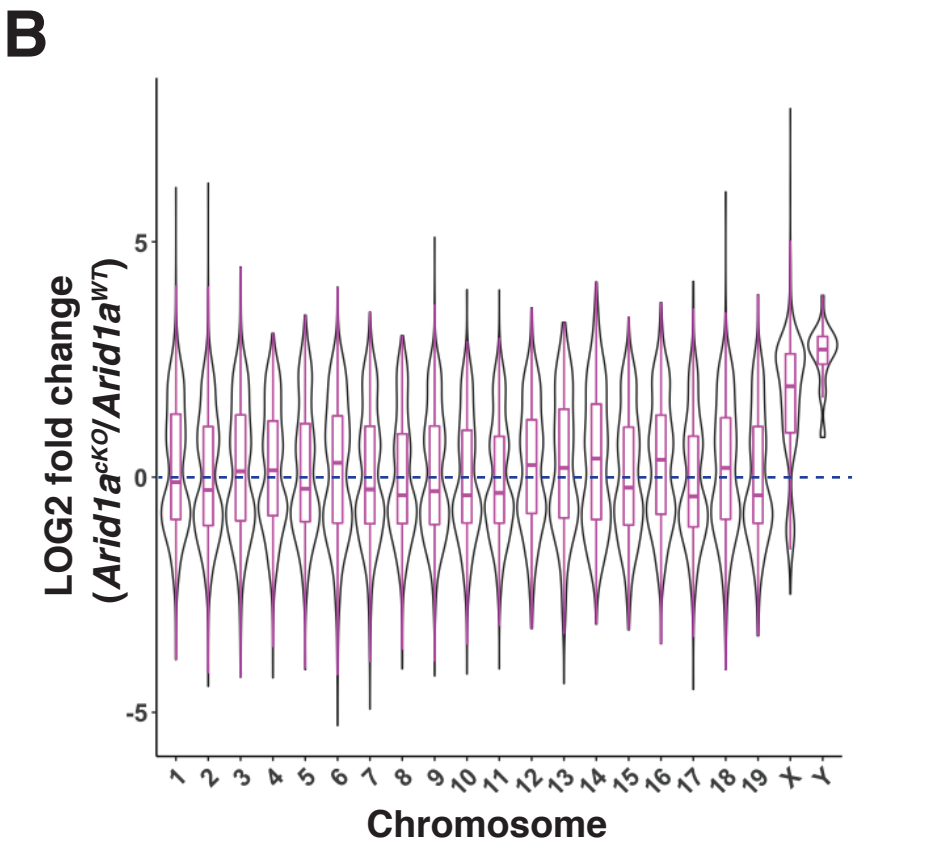
B
LOG2 fold change
(Arid1a^cKO/Arid1a^WT)
5
0
-5
1
2
3
4
5
6
7
8
9
10
11
12
13
14
15
16
17
18
19
X
Y
Chromosome

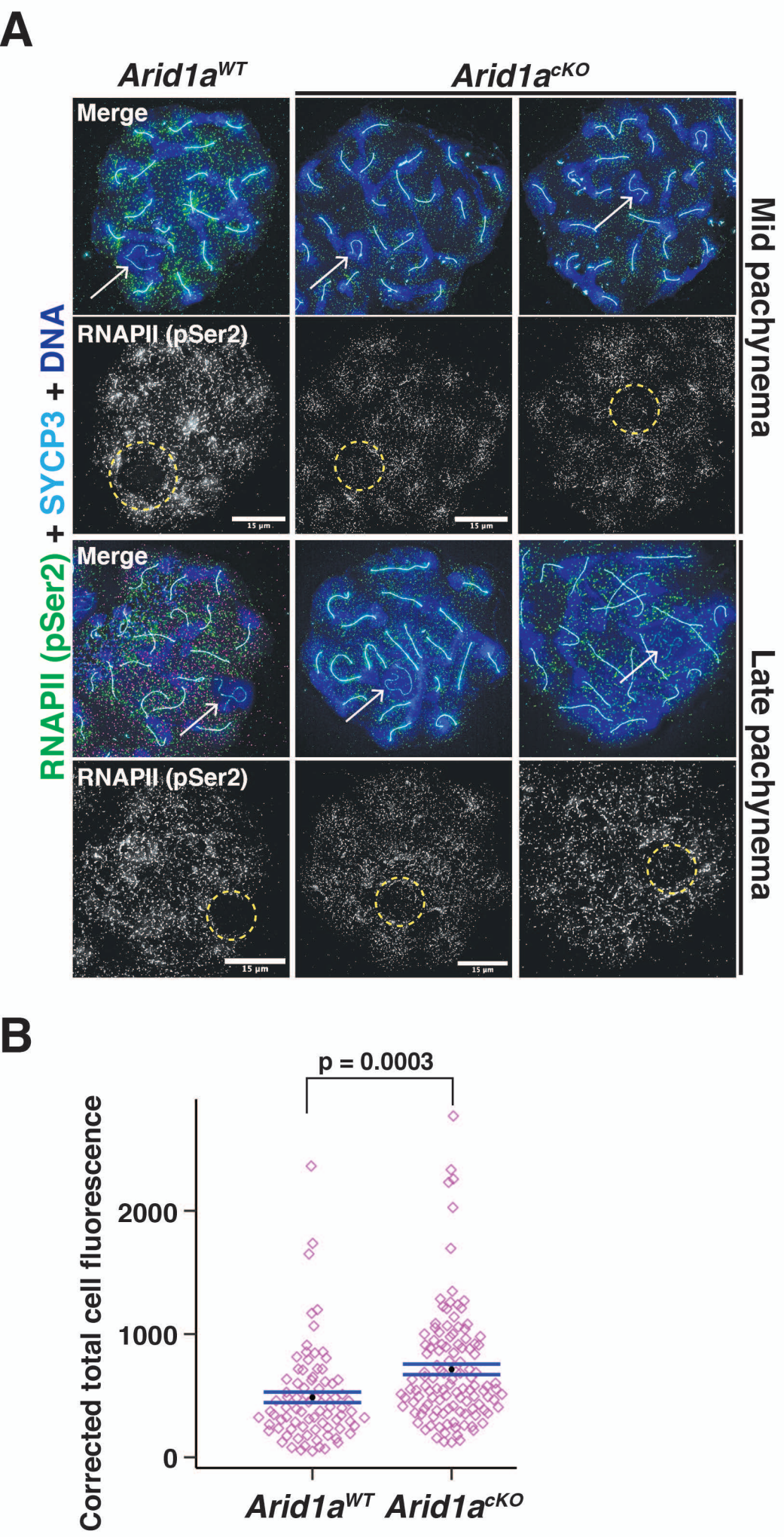
A
Arid1a^WT
Arid1a^cKO
Merge
RNAPII (pSer2)
RNAPII (pSer2) + SYCP3 + DNA
Mid pachynema
Late pachynema
15 µm
B
p = 0.0003
Corrected total cell fluorescence
2000
1000
0
Arid1a^WT
Arid1a^cKO

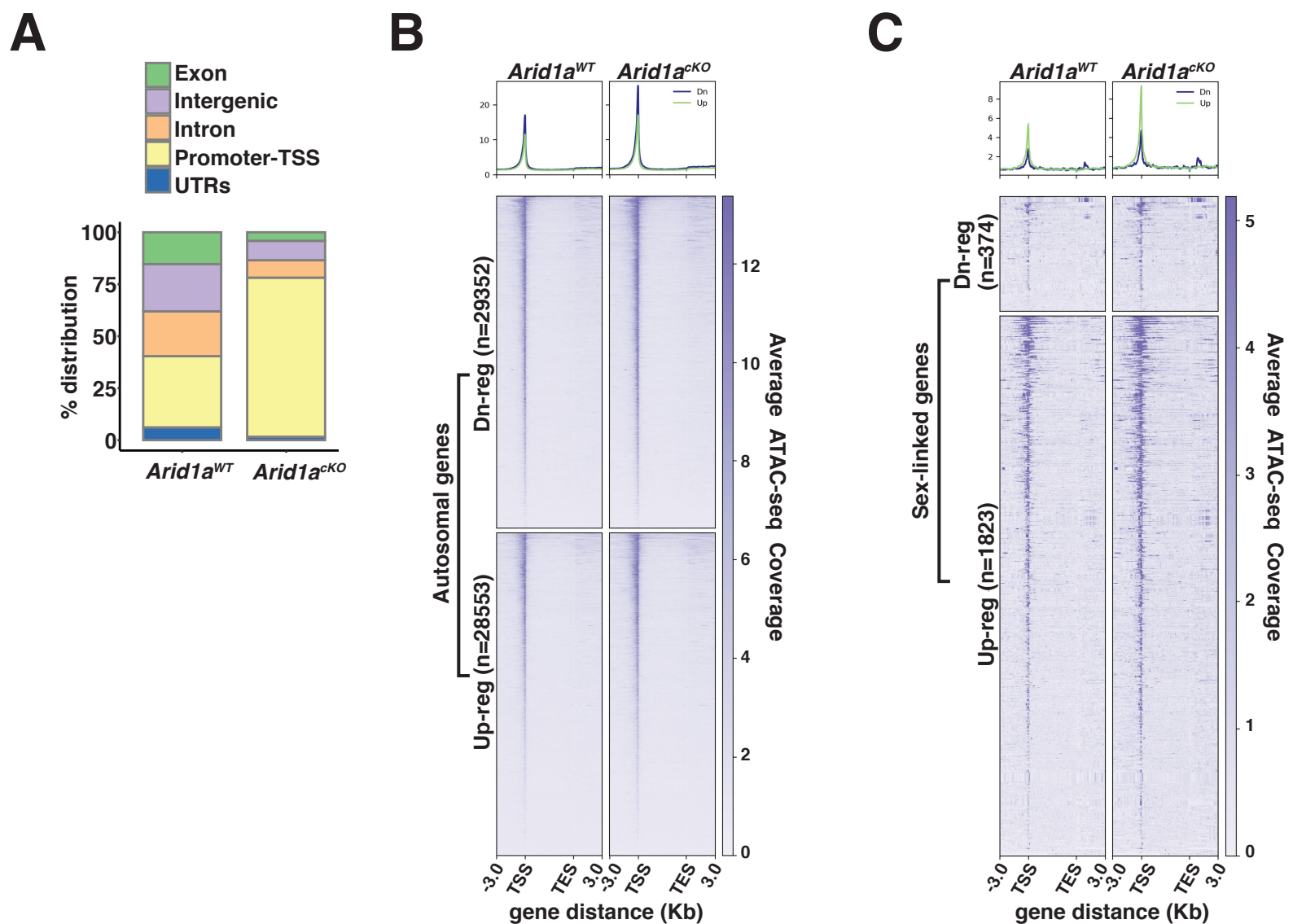
A
Exon
Intergenic
Intron
Promoter-TSS
UTRs
% distribution
100
75
50
25
0
Arid1a^WT
Arid1a^cKO
B
Arid1a^WT
Arid1a^cKO
Dn
Up
Autosomal genes
Dn-reg (n=29352)
Up-reg (n=28553)
Average ATAC-seq Coverage
-3.0
TSS
TES
3.0
gene distance (Kb)
C
Arid1a^WT
Arid1a^cKO
Dn
Up
Sex-linked genes
Dn-reg (n=374)
Up-reg (n=1823)
Average ATAC-seq Coverage
-3.0
TSS
TES
3.0
gene distance (Kb)

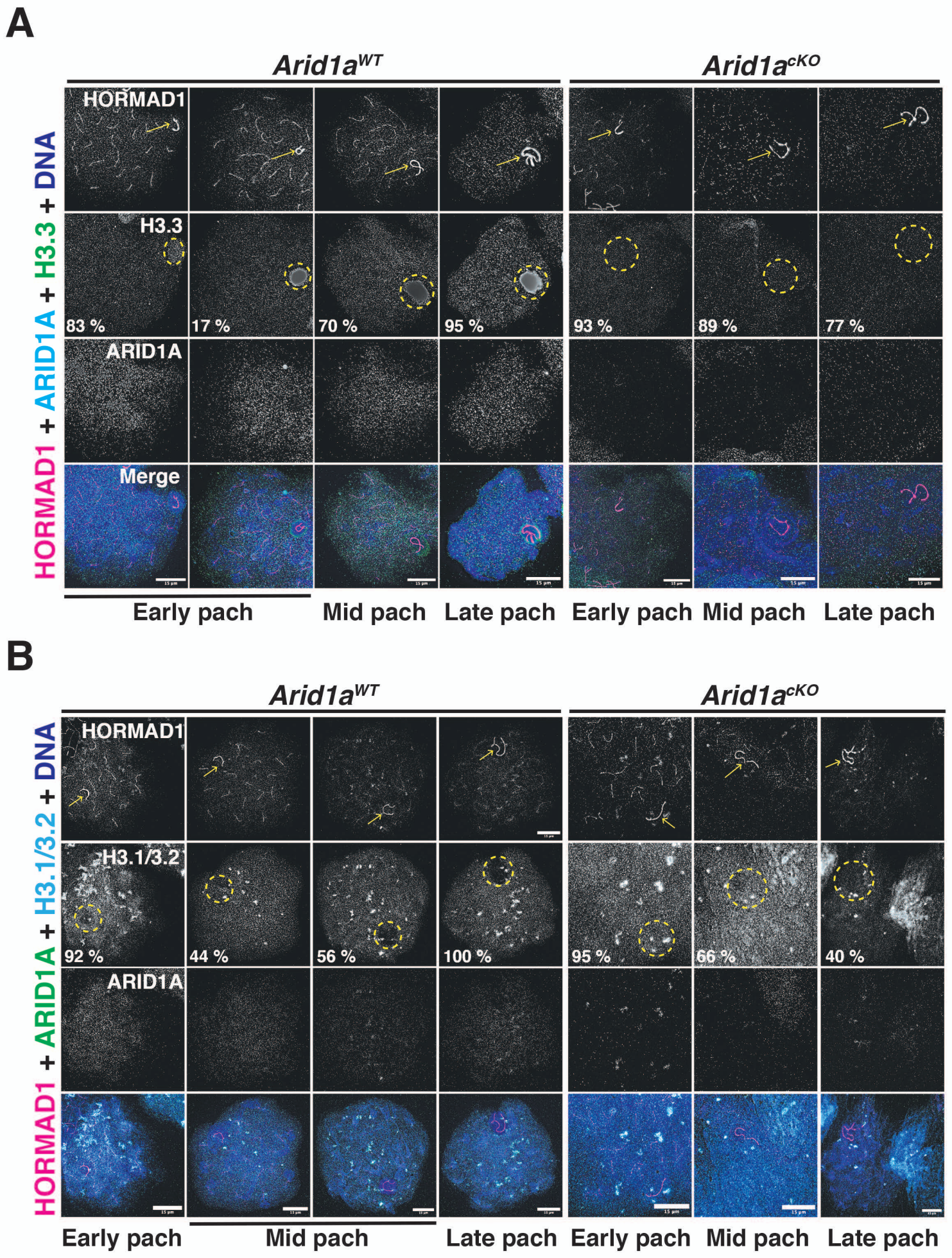
A
Arid1a^WT
Arid1a^cKO
HORMAD1 + ARID1A + H3.3 + DNA
HORMAD1
H3.3
ARID1A
Merge
83 %
17 %
70 %
95 %
93 %
89 %
77 %
Early pach
Mid pach
Late pach
Early pach
Mid pach
Late pach
B
Arid1a^WT
Arid1a^cKO
HORMAD1 + ARID1A + H3.1/3.2 + DNA
HORMAD1
H3.1/3.2
ARID1A
92 %
44 %
56 %
100 %
95 %
66 %
40 %
Early pach
Mid pach
Late pach
Early pach
Mid pach
Late pach

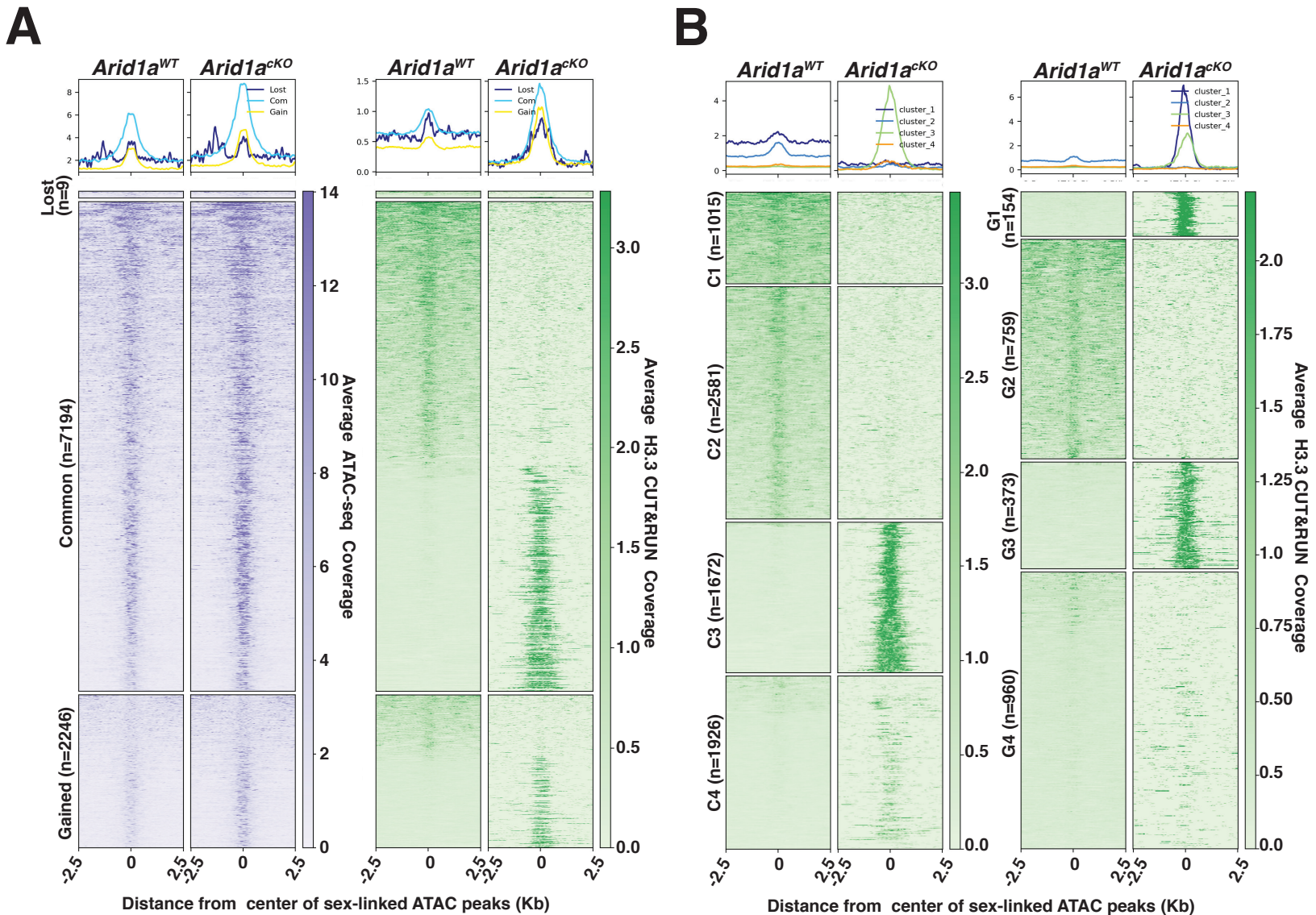
A
Arid1a^WT
Arid1a^cKO
Lost
Com
Gain
Lost (n=9)
Common (n=7194)
Gained (n=2246)
Average ATAC-seq Coverage
Average H3.3 CUT&RUN Coverage
Distance from center of sex-linked ATAC peaks (Kb)
B
cluster_1
cluster_2
cluster_3
cluster_4
C1 (n=1015)
C2 (n=2581)
C3 (n=1672)
C4 (n=1926)
G1 (n=154)
G2 (n=759)
G3 (n=373)
G4 (n=960)
Average H3.3 CUT&RUN Coverage
Distance from center of sex-linked ATAC peaks (Kb)

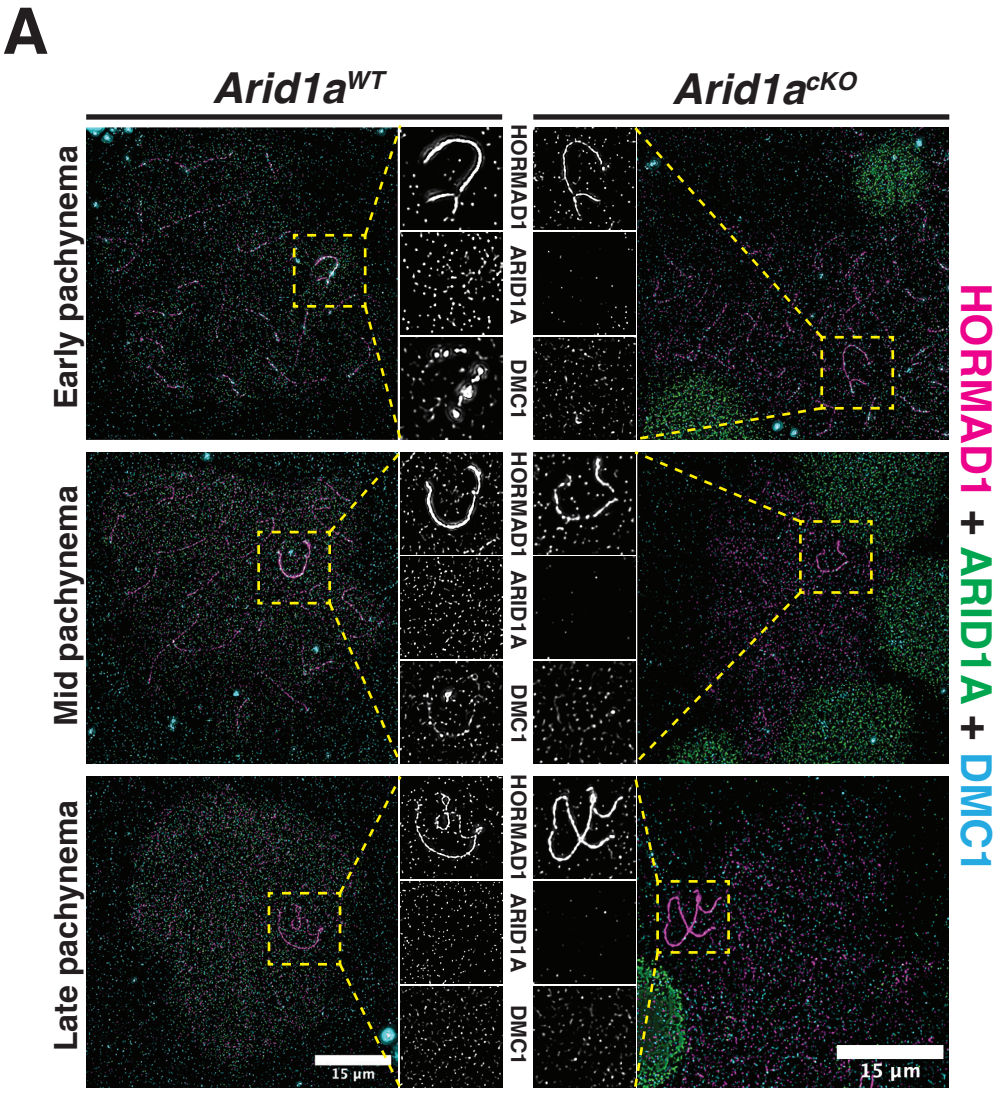
A
Arid1a^WT
Arid1a^cKO
Early pachynema
Mid pachynema
Late pachynema
HORMAD1
ARID1A
DMC1
HORMAD1 + ARID1A + DMC1
15 µm
15 µm

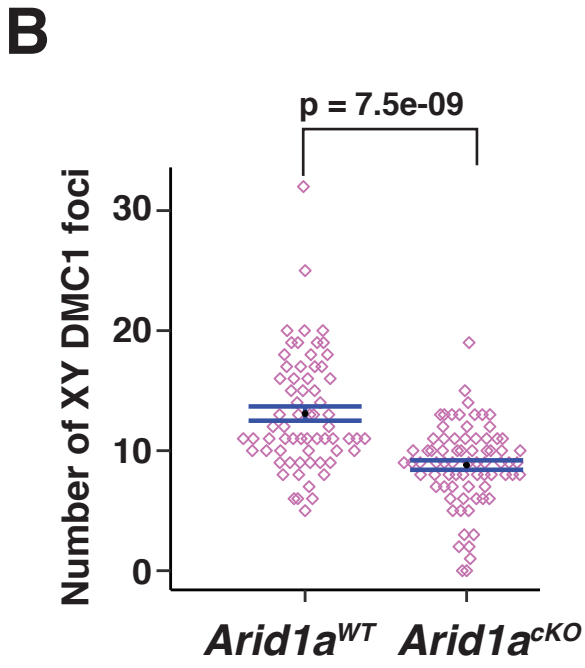
B
p = 7.5e-09
Number of XY DMC1 foci
30
20
10
0
Arid1a^WT
Arid1a^cKO

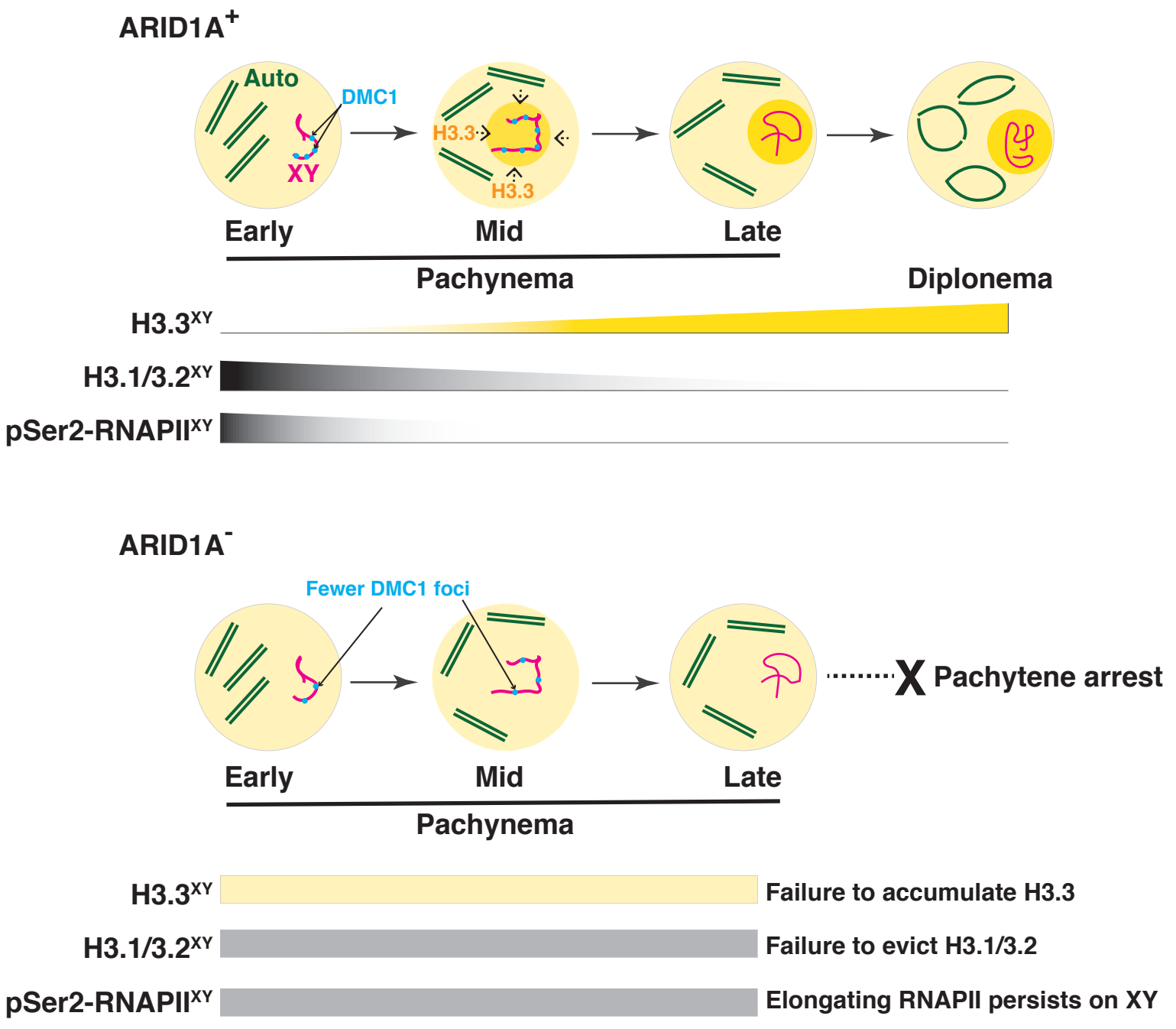
ARID1A+
Auto
DMC1
XY
H3.3
H3.3
Early
Mid
Late
Pachynema
Diplonema
H3.3XY
H3.1/3.2XY
pSer2-RNAPIIXY
ARID1A-
Fewer DMC1 foci
X Pachytene arrest
Early
Mid
Late
Pachynema
H3.3XY
Failure to accumulate H3.3
H3.1/3.2XY
Failure to evict H3.1/3.2
pSer2-RNAPIIXY
Elongating RNAPII persists on XY